

# Persistence B-Spline Grids: Stable Vector Representation of Persistence Diagrams Based on Data Fitting

Zhetong Dong, Hongwei Lin\*, Chi Zhou

School of Mathematical Sciences, Zhejiang University

**Abstract:** Over the last decades, many attempts have been made to optimally integrate machine learning (ML) and topological data analysis. A prominent problem in applying persistent homology to ML tasks is finding a vector representation of a persistence diagram (PD), which is a summary diagram for representing topological features. From the perspective of data fitting, a stable vector representation, *persistence B-spline grid* (PB), is proposed based on the efficient technique of progressive-iterative approximation for least-squares B-spline surface fitting. Meanwhile, we theoretically prove that the PB method is stable with respect to the metrics defined on the PD space, i.e., the  $p$ -Wasserstein distance and the bottleneck distance. The proposed method was tested on a synthetic dataset, datasets of randomly generated PDs, data of a dynamical system, and 3D CAD models.

**Keywords:** Machine Learning, Persistent Homology, B-Spline Surface, Progressive-Iterative Approximation

## 1 Introduction

In the advent of the big-data era, one of the significant tasks is to infer the topological structures of data at different scales. Today, *persistent homology* [1, 2] provides us a robust tool to capture topological features of data, such as holes based on the homology theory. These multidimensional homological features are represented as a *persistence diagram* (PD) or a *barcode* [3]. Moreover, persistent homology has been applied successfully to deal with various practical problems in different scientific and engineering fields, such as biochemistry [4, 5] and information science [6, 7]. Meanwhile, the machine learn-

---

\*Email: hwlin@zju.edu.cn

ing (ML) community has shown growing interest in combining traditional ML methods and the current techniques of computational topology [8–10]. In the applications of ML, the distance metrics (the *p-Wasserstein distance* and the *bottleneck distance*) of two PDs proposed by Cohen-Steiner et al. [11] make it possible to compute the distance matrix in the tasks of clustering and classification. Because it usually costs a lot of time to compute the distance mentioned above, questions arises to find an efficient approach to compute the distance, and [12] proposed an alternative. On the other hand, to apply the topological summary, i.e., PD, to ML problems, it is supposed to extend the representation of topological features into the form of vectors which have the property of stability with respect to the distance of PDs. A representation of vector has advantages of being easy to compute the distance and being available for more ML tools than the form of distance matrix. For instance, a vectorizing representation of PD is welcomed by support vector machine (SVM), a commonly used ML tool requiring vectors as input. Overall, it provides a clear motivation to represent PDs by stable vectors.

## 1.1 Related Work

Many approaches have been proposed to transform PDs into vectors. Often these attempts are developed when studying practical applications. For example, while researching the cortical thickness measurements of the human cortex for the study of Alzheimer’s disease, Pachauri et al. [13] rasterized PDs on a regular grid, computed a kernel density estimation to generate the concentration map using the Gaussian kernel, and vectorized concentration maps for SVM training. However, the relationship between the kernel distance they used and the *p-Wasserstein distance* or *bottleneck distance* is unclear. Carrière et al. (2015) [14] computed the matrix of distances between each pair of points on a PD, sorted the distances in the descending order to form a vector, and truncated the vector to maintain a fixed length. This process was proved to be stable with respect to the *bottleneck distance* in the sense of 2-norm and  $\infty$ -norm of vector space.

From the perspective of algebraic polynomials, Di Fabio and Ferri (2015) [15] proposed a method for shape retrieval. They transformed a PD into a set of complex numbers and constructed a complex-coefficient polynomial with complex numbers as its roots. The transformed vector was generated by ordering the coefficients of the polynomial. Their study, however, does not mention the stability properties of such method. Adcock et al. (2016) [16] identified the ring of algebraic functions on a barcode and described the algebra generators for shape analysis. Furthermore, Kališnik (2018) [17]

proved the instability of the algebraic functions proposed by Adcock et al. (2016) [16]. They identified tropical coordinates on the barcodes space and proved the stability of this representation with respect to the bottleneck distance and  $p$ -Wasserstein distance.

From the perspective of statistics, Mileyko et al. [18] developed probability measures on the space of PDs. Bubenik [19] defined a functional representation in a Banach space, persistence landscapes, induced by persistence modules [2]. Persistence landscape satisfies the proposed  $\infty$ -landscape stability and  $p$ -landscape stability with the same condition as the stability of the  $p$ -Wasserstein distance [20]. However, it is difficult to interpret the representation of persistence landscapes.

Inspired by a heat diffusion problem with a Dirichlet boundary condition, Reininghaus et al. [21] proposed the persistence scale space kernel (PSSK), a framework of multi-scale kernel that is  $W - 1$  stable. They also showed that this kernel is an additive kernel. Because of its additive property on PDs, this kernel is unstable for higher values of  $p$ , where  $1 < p \leq \infty$ . Here, when  $p = \infty$ , the distance is the bottleneck distance. Meanwhile, for obtaining an interpretable result, an easy approach was used by Rouse et al. [22]. They constructed a finite grid in the birth-persistence coordinates, quantized the birth-persistence pairs to the grid, counted the number of pairs at each grid, and rearranged the counts into a vector in the order of the grid. This method is sensitive to the division of the grid region, which might not be robust with respect to noise, and the importance of the points in a PD was not considered.

Persistence images (PIs) proposed by Adams et al. [23] combined the idea of the kernel framework of Reininghaus et al. [21] and the idea of “pixel” counting of Rouse et al. [22]. First, a product of a two-dimensional Gaussian distribution and a weighted function is assigned to each point in the birth-persistence coordinates, and they are added up to form a persistence surface. Then, the domain is divided by a regular grid into regular small regions called pixels. The integral value of a persistence surface is computed on each pixel to generate an image. Note that if the variance  $\sigma$  approaches zero, Gaussian function tends to the Dirac delta, and the integral value on each pixel tends to be the sum of weighted function values of the points on the pixel, which degenerates into the weighted sum given by Rouse et al. [22]. Among their advantages, PIs (a) allow users to assign a weight on each point in a PD to adjust the importance of the point, and (b) provide an efficient and easily understandable approach to vectorize PDs for ML tasks. Similar to the case of the kernel in Reininghaus et al. (2015) [21], the persistence surface of PI is additive, causing a disadvantage in using this technique. In fact, as Reininghaus et al. (2015) [21] stated in Theorem 3 of their publication, for two

distribution surfaces  $f_1$  for  $PD_1$  and  $f_2$  for  $PD_2$ , if  $f_1 + f_2$  is the distribution surface of  $PD_1 \cup PD_2$ , then the method to form the distribution surface is additive. If  $1 < p \leq \infty$ , the increasing magnitude of the additional distribution surfaces cannot be bounded by the  $p$ -Wasserstein distance. As an example, consider an empty PD denoted as  $\emptyset$  with its distribution surface  $f = 0$ , and a PD denoted as  $D$  with its distribution surface  $g$ . Assume that there is merely one point over the diagonal on  $D$ . Let  $\bar{D}$  be a finite union of  $n$   $D$ 's, that is,  $\bar{D} = \bigcup_{i=1}^n D^{(i)}$ . The distribution surface is given by  $\bar{g} = \sum_{i=1}^n g^{(i)}$ . Note that

$$\|\bar{g} - f\|_p = n\|g\|_p, \quad W_p(\bar{D}, \emptyset) = n^{\frac{1}{p}} W_p(D, \emptyset), \quad \text{where } p > 1. \quad (1)$$

For a fixed  $p$ , the term  $\|\bar{g} - f\|_p$  cannot be controlled by the form  $C \cdot W_p(\bar{D}, \emptyset)$  as  $n$  increases, where  $C$  is a non-negative constant. Whence, PIs preserve the instability for higher values of  $p$ , where  $1 < p \leq \infty$ .

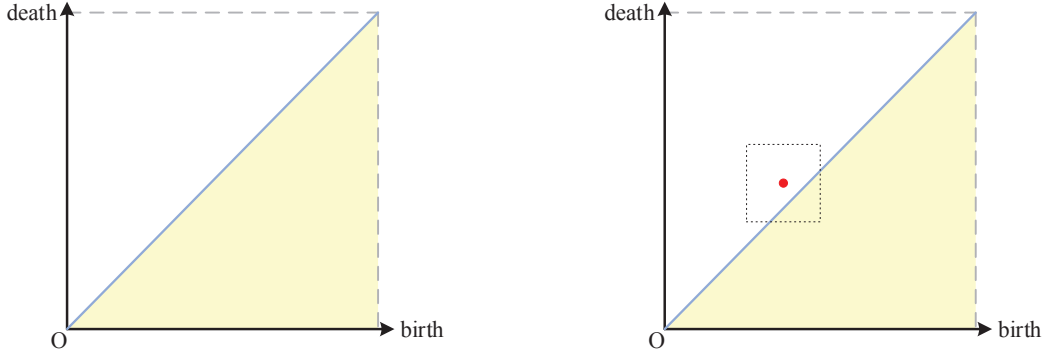


Figure 1: Left figure: an empty PD. Right figure: the constructed PD  $\bar{D}$  where there is  $n$  topological features with the same birth and death coordinates in the marked point inside the dashed region.

Recently, kernel methods have been widely developed for finding an appropriate measurement of distance of PDs. Setting up a kernel is an effective framework for PD representation. The main idea of the framework of kernel methods is to transform PDs into probability density functions so that the distance between the PDs can be evaluated. Kernels also play an important role in ML models, such as kernel SVM, principal components analysis, and spectral clustering. As mentioned above, PSSK proposed by Reininghaus et al. [21] is a kernel. From the perspective of kernel, a PD is transformed into a multiscale function by convolution with Gaussian kernels together with scale parameters. Kusano et al. [24] summarized previous works based on kernel

functions and developed persistence weighted Gaussian kernel (PWGK), a statistical framework of the kernel method that vectorizes PDs by employing kernel embedding of measures into reproducing kernel Hilbert spaces. In PWGK, the topological features with short persistence have a slight impact, because these features are considered as noise. The property of random Fourier features is used to efficiently compute PWGK. Kusano et al. also proved the stability of PWGK with respect to the Hausdorff distance between data.

Sliced Wasserstein Kernel (SWK) for PDs was proposed by Carrière et al. (2017) [25]. The points on PDs are projected on a series of lines passing through the origin, and the slopes of these lines are adjusted. By SWK, the distance of PDs is measured as the distances between the projected points on these lines. SWK is a negative semi-definite kernel, and it is stable with respect to  $W_1$  distance of PD. Le & Yamada [26] employed another definite kernel, the persistence Fisher kernel, which has the advantages of stability and infinite divisibility. They transformed a PD into a normalized probability density function. The square-root of this function forms a unit Hilbert sphere so that the Fisher information metric is used to define an inner product metric to generate the kernel. Other kernel methods ([27], [28]) are being developed to be incorporated into kernel-based ML models.

## 1.2 Contribution of the Present Study

From the perspective of data fitting and approximation, it is noticed that the weighted kernel framework can be thought to interpolate with basis functions the “importance” value assigned on each PD point given by weighting functions. To overcome the instability due to additive property [21] of kernels and separate “importance” values from the basis, a data fitting framework is proposed based on the B-spline surface, and bounded “importance” values, named *eminence functions*, are redesigned to guarantee the stability with respect to the  $p$ -Wasserstein distance and the bottleneck distance. The information of PDs is encoded into the finitely dimensional vectors produced by the control grid of the *persistence B-spline surface* (PB), so that one can reconstruct precisely the persistence surface from the vectors. To efficiently compute the persistence B-spline surface, the technique of *progressive-iterative approximation for least squares B-spline surface fitting* (LSPIA) [29] is then employed to robustly generate the vectors. Generally, the advantages of the PB method include that it is

- stable with respect to the  $p$ -Wasserstein distance and the bottleneck distance,

- efficient to compute and understandable,
- flexible to design the “importance” values for different practical tasks,
- and invertible to recover the surfaces from vectors.

## 2 Background

The features, such as connected components, loops, and voids, remain invariant under a proper geometric transformation. In algebraic topology, homology is a mathematical formalism to measure these “holes” of different dimensions. Given a topological space  $X$ , the elements of  $n$ -dimensional homology group  $H_n(X)$  represent homology classes describing  $n$ -dimensional holes. Since  $H_n(X)$  is an abelian group, the Betti number is defined to be the rank of abelian group  $H_n(X)$ , denoted as  $\beta_n$ . Intuitively,  $\beta_0, \beta_1$  and  $\beta_2$  suggest respectively the number of connected components, one-dimensional loops and two-dimensional voids that a topological space contains. However, homology enables a fast matrix reduction algorithm working with module 2 coefficients to compute the reduced Betti numbers. A preliminary about homology is attached in Appendix A, and for more knowledge about computational homology, readers can refer to the book [30].

In the real world, one samples from a continuous object to obtain a discrete point cloud. Meanwhile, there exist measurement errors and inevitable sampling noises. The problem arises of inferring the topological structures of point clouds. *Persistent homology* provides a tool by which the topological features of different dimensions can be captured with their importances marked by their *persistences*. The most important aspect is that it has stability with respect to small perturbations and noises. It is customary to use the *Vietoris-Rips complex* (V-R complex) in the vast toolkit of topology to set up the structure of *simplicial complex* [31]. One can take the V-R complex as an example. The V-R complex contains the points  $p_i$  as vertices and  $n$ -simplices generated by  $n + 1$  points of which any pair of closed balls has a nonempty intersection. Given a series of parameters  $\epsilon_0 \leq \epsilon_1 \leq \dots \leq \epsilon_m$ , one obtains a nested sequence

$$VR(\epsilon_0) \subseteq VR(\epsilon_1) \subseteq \dots \subseteq VR(\epsilon_m),$$

which is called a *filtration*. We have an inclusion between  $VR(\epsilon_i)$  and  $VR(\epsilon_{i+1})$ . It induces a homomorphism  $H_n(VR(\epsilon_i)) \rightarrow H_n(VR(\epsilon_{i+1}))$  for each  $n$ . We have

$$H_n(VR(\epsilon_0)) \rightarrow H_n(VR(\epsilon_1)) \rightarrow \dots \rightarrow H_n(VR(\epsilon_m)).$$

As “time”  $i$  goes by, some new homological classes emerge, and some disappear because they become the boundary of a higher chain or merge with other classes. Vividly,

a homological class is *born* at  $i$  if it emerges in  $H_n(VR(\epsilon_i))$ , and it *dies* at  $j$  if it disappears in  $H_n(VR(\epsilon_j))$ . Its lifetime ( $j - i$ ) is the *persistence* of the homological class. If a homological class never dies, its persistence is set to infinity. PDs and barcodes [3] are two commonly used ways to represent the persistence of homological features. The pairs  $(i, j)$  for  $n$ -dimension are marked in the birth-death coordinates on the  $\mathbb{R}^2$  plane. Because  $i \leq j$  for each pair, it is necessary that all the points on a PD are above or exactly on the diagonal line. In practice, the points close to diagonal line are subjectively regarded as noise.

Finally, the filtration of functions and stability of PDs are introduced. Given a topological space  $\mathbb{X}$ ,  $f : \mathbb{X} \rightarrow \mathbb{R}$  is a scalar function. The *sublevel set* is defined by  $f^{-1}(-\infty, a] = \{x \in \mathbb{X} | f(x) \leq a\}$  consisting of all points with its scalar value at most  $a$ . It induces a filtration of the topological space  $\mathbb{X}$  by the function  $f$ , and, if there is a series of scalar values  $a_0 \leq a_1 \leq \dots \leq a_m$ , then

$$f^{-1}(-\infty, a_0] \subseteq f^{-1}(-\infty, a_1] \subseteq \dots \subseteq f^{-1}(-\infty, a_m]$$

In the sense of the distance function  $d$  on the point set  $P$ , one can also determine a V-R complex over  $P$ . For a function  $f : \mathbb{X} \rightarrow \mathbb{R}$ , if some small perturbations occur, what happens to the PD? The stability of PDs was studied by Cohen-Steiner et al. [11]. With some mild assumptions for the function  $f$  and  $\tilde{f}$  with respect to small perturbations, the *p-Wasserstein distance* of two corresponding PDs can be controlled by a certain term of  $L_\infty$ -norm of  $|f - \tilde{f}|$ . The metrics to measure the similarity of two PDs are the *p-Wasserstein distance* and the *bottleneck distance*, defined as follows.

**Definition 2.1.** *The p-Wasserstein distance between  $PD_1$  and  $PD_2$  is given by*

$$W_p(PD^{(1)}, PD^{(2)}) = \inf_b \left( \sum_{u \in PD^{(1)}} \|u - b(u)\|_\infty^p \right)^{1/p}$$

and the bottleneck distance is given by

$$W_\infty(PD^{(1)}, PD^{(2)}) = \inf_b \sup_{u \in PD^{(1)}} \|u - b(u)\|_\infty$$

where  $u$  is a point in  $PD^{(1)}$ ,  $b$  is a bijection between  $PD^{(1)}$  and  $PD^{(2)}$ , and  $W_\infty$  denotes the bottleneck distance.

### 3 Method and Algorithm

Our goal is to introduce a vectorizing representation of PDs. We notice that in some methods such as kernel methods and PIs, a point in a PD is usually associated with a

basis function, and the weighted summation of these functions is computed to generate a kernel or a persistence surface. In the view of data fitting, it can be understood as the form in which the “importance” values of a point in a PD, given by weight values, are interpolated by basis functions such as Gaussian functions. As explained in section 1, these methods remain to be  $W_1$  stable, but unstable for higher values of  $p$  unless the number of points in a PD is restricted. To attempt a new alternative of interpolation instead of interpolation based on radial basis functions, the idea appears to approximate the PD points together with their “importance” values by a B-spline surface. The advantage of using B-spline is that information of a B-spline surface is encoded in the control points, a control grid, which can be transformed into a finitely dimensional vector. And the structure of a B-spline surface is different from the persistence surface generated by a summation of basis functions. Thus, it is possible to prove  $W_p$  stability of the vectorizing representation. However, the traditional method to obtain a B-spline surface approximating data points is to solve a system of linear equations, which causes numerical instability of the solution and a huge time spending. To compute the B-spline surface efficiently and robustly, the technique of progressive-iterative approximation for least squares B-spline surface fitting (LSPIA) is exactly what we need. Therefore, an effective method of PD vectorization based on B-spline interpolation and LSPIA is proposed.

In this section, the persistence B-spline grid to vectorize PDs is introduced. A PD is transformed into the birth-persistence coordinates, and an *eminence value* is assigned to each point in a PD to mark its importance. A *persistence B-spline surface* is defined to fit the data points in 3D Euclidean space. The surface reflects local tendencies of the eminence on each topological feature due to the local support property of the B-spline basis, i.e., each basis has a small closed interval as its support set. Eventually, the algorithm to compute, efficiently and robustly, the persistence B-spline surface by the technique of LSPIA is provided.

### 3.1 Construction of Persistence B-Spline Surfaces

First, the coordinates should be handled because the points scattered above the diagonal line. [32] offers an alternative to transform a birth-death coordinate into a (birth+death)-persistence coordinate. However, for the purpose of comparing with PIs, a PD is transformed into the birth-persistence coordinates. Thus, a transformation  $\phi$  is defined. For each  $(x_l, y_l)$  in a PD, let  $\phi : \mathbb{R}^2 \rightarrow \mathbb{R}^2$  be a linear transform satisfying  $\phi(x, y) = (x, y - x)$ .

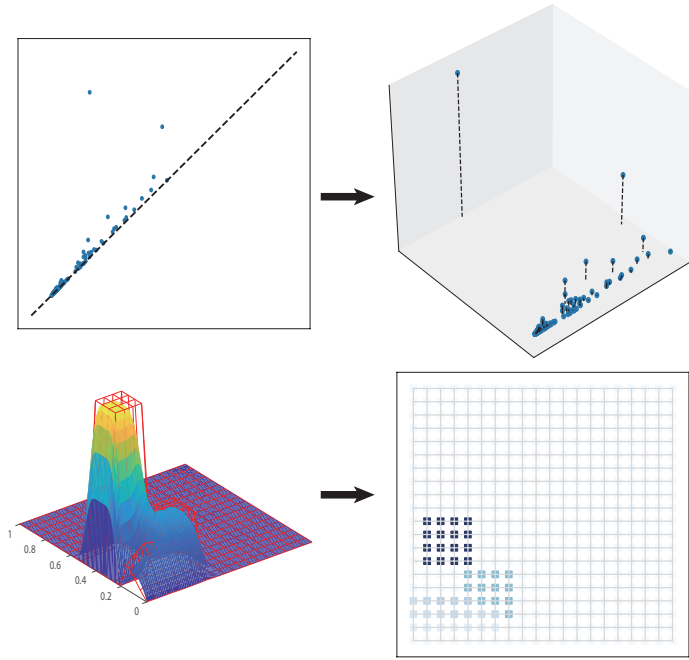


Figure 2: Pipeline: A persistence diagram is transformed in the birth-persistence coordinates and an “eminence” value is assigned on each point to illustrate the importance of the topological feature. Then, the 3D data points are fitted by a cubic uniform B-spline surface with the technique of LSPIA. Finally, the control grid (the red grid in the bottom-left figure) is obtained to generate a vector by concatenating rows of  $z$ -coordinates of the control grid. The persistence B-spline grid (bottom right) is defined by the matrix formed by the  $z$ -coordinates of the control points .

In practice, a collection of PDs, denoted as  $\{PD\}_\Lambda$ , obtained by V-R complex, usually contains a finite number of points with finite persistence.<sup>1</sup> One can consider points in a bounded region on a PD, and let  $m$  be a positive constant properly greater than the maximum of the  $x$  and  $y$  coordinates for each point in all PDs, i.e.  $\max_\Lambda \{\max_{(x,y) \in PD} \{x, y\}\}$ . And then, we consider the points in the region  $[0, m]^2$  on a PD, and define a normalizing function  $c(x, y) = (x/m, y/m)$  from  $\mathbb{R}^2$  to  $[0, 1]^2$ . The domain in birth-persistence coordinates is normalized by the normalizing function. Denote

$$(s_l, t_l) = c \circ \phi(x_l, y_l) \quad (2)$$

<sup>1</sup> Although there exists a topological feature with infinite persistence that represents the connect- edness of the whole simplicial complex in  $H_0$  PDs, to compute PDs of the corresponding reduced  $H_0$  homology gets rid of this challenge.

for each  $(x_l, y_l)$  in a PD. Therefore, the normalized birth-persistence coordinates  $(s_l, t_l)$  are obtained.

Since the importance of each point in a PD is illustrated variously in different tasks, an eminence value  $z_l$  is assigned on each point in a PD by an *eminence function*  $\mathcal{E}(x, y)$ . The principle of designing an eminence function is derived from the understanding of topological features with different persistence. Persistence of points and the local density of points should be taken into consideration when an eminence function is designed. Generally, the points close to the diagonal line are thought to be noise, marked with a small eminence value, and, on the contrary, the points far away from the diagonal line are marked with a large eminence value. Furthermore, a point in a PD surrounded by much more points might be regarded to be more important, marked with a larger eminence value. Provided for the eminence functions to measure the eminence value by persistence, the function  $f$  is a monotonically increasing function passing through the origin. A Lipschitz function is a better choice of the function  $f$ . One can take

$$f(x) = \begin{cases} x & x \leq L \\ L & x > L \end{cases} \quad (3)$$

where  $L$  is a positive constant integer. To consider the local density of a point in a PD, for a point  $(x_l, y_l)$  in a PD, we count the number of points in an  $\varepsilon$ -ball of the point  $(x_l, y_l)$ , denoted as  $n_\varepsilon$ , and a bound  $M$  is set for  $n_\varepsilon$ . Finally, we define  $\mathcal{E} : \mathbb{R}^2 \rightarrow \mathbb{R}$  to be

$$z_l := \mathcal{E}(x_l, y_l) = \begin{cases} n_\varepsilon f(y_l - x_l) & 1 \leq n_\varepsilon \leq M \\ M f(y_l - x_l) & n_\varepsilon > M \end{cases} \quad (4)$$

where  $n_\varepsilon$  is the number of points contained by an  $\varepsilon$ -open ball of  $(x_l, y_l)$  in a PD, and  $M$  is a positive constant integer. Notice that the eminence function  $\mathcal{E}$  must be bounded. One may choose a more complicated eminence function according to the principle.

And next, a uniform cubic B-spline surface with a collection of control points  $\{(s_i, t_j, p_{ij})\}_{i,j=1}^h$  is used to fit the data points  $(s_l, t_l, z_l)$ , where each  $(s_i, t_j)$  is a knot of an  $h \times h$  uniform grid in  $[0, 1]^2$ . Precisely, the following definitions are given.

**Definition 3.1** (Persistence B-Spline Surface). *Given a PD, for each  $(x_l, y_l)$  in the PD, after transformation, one gets  $(s_l, t_l)$ . Furthermore,  $z_l$  (8) is the assigned eminence value on each  $(s_l, t_l)$ . A uniform cubic B-spline surface with its uniform control grid  $\{(s_i, t_j, p_{ij})\}_{i,j=1}^h$  satisfying*

$$\min_{\{p_{ij}\}} \sum_l \|z_l - S_p(s_l, t_l)\|_2$$

$$s.t. \quad S_p(s, t) = \sum_{i=0}^h \sum_{j=0}^h p_{ij} B_i(s) B_j(t) \quad s, t \in [0, 1]$$

is a persistence B-spline surface for the corresponding PD, where  $B_i(\cdot)$  and  $B_j(\cdot)$  are the uniform cubic B-spline basis determined by uniform knot sequences.  $\{p_{ij}\}$  are the z-coordinates of the control points.

The control points of PB surface provide a flexible method to vectorize the PDs.

**Definition 3.2** (Persistence Grid & Persistence Vector). *If  $S_p(s, t)$  is the persistence B-spline surface for a PD, then the z-coordinate of the control points,  $\{p_{ij}\}_{i,j=1}^n$ , is called the persistence grid of a PD. A vector generated by arranging it with the lexicographic order,*

$$\tilde{\mathbf{Z}} = (p_{11}, p_{12}, \dots, p_{1h}, p_{21}, \dots, p_{hh})^T \in \mathbb{R}^{h^2},$$

is called the persistence vector of a PD.

Especially when one deals with the PDs for  $H_0$ , in which the birth coordinate  $s_l$  for each point in PDs is zero, PB makes it possible to fit the  $\{(t_l, z_l)\}$  data set by the uniform cubic B-spline curves.

### 3.2 Algorithm and LSPIA

The universal method to obtain a B-spline surface fitting data points in the space is to solve a system of linear equations. According to definition 3.1, one has the following linear equations:

$$\mathbf{B}\tilde{\mathbf{Z}} = \mathbf{Z}, \tag{5}$$

where  $\mathbf{B}$  is the cubic B-spline basis matrix, and

$$\begin{aligned} \tilde{\mathbf{Z}} &= (p_{11}, p_{12}, \dots, p_{1h}, p_{21}, \dots, p_{hh})^T, \\ \mathbf{Z} &= (z_1, z_2, \dots, z_k)^T. \end{aligned}$$

Normally,  $\mathbf{B}$  is singular. An alternative approach of computing the minimum-norm least-squares solution of the linear equations is to determine the Moore-Penrose pseudo-inverse of the matrix  $\mathbf{B}$ . Unfortunately, it suffers from numerical instability. To remain the efficiency and numerical robustness to work out  $\{p_{ij}\}$ , a flexible and efficient tool, LSPIA, is employed from scientific computation to avoid the expensive time cost and to keep the robustness.

Precisely, given a data set  $\{\mathbf{Q}_l\}_{l=1}^k$  where each  $\mathbf{Q}_l = (s_l, t_l, q_l)$ , assume that each  $(s_l, t_l)$  is in the domain  $[0, 1]^2$ . Before the iteration, the control points  $\{\mathbf{P}_{ij}\}_{i,j=0}^n$ , where

$\mathbf{P}_{ij} = (s_i, t_j, p_{ij})$ , are initialized. For each  $\mathbf{P}_{ij}^{(0)} = (s_i, t_j, p_{ij}^{(0)})$ , let  $\{(s_i, t_j)\}$  be the vertices of a uniform grid on  $[0, 1]^2$  and  $p_{ij}^{(0)} = 0$ . The initial surface is constructed by

$$S^{(0)}(s, t) = \sum_{i=0}^n \sum_{j=0}^n p_{ij}^{(0)} B_i(s) B_j(t) \quad s, t \in [0, 1]$$

Let  $\delta_l^{(0)} = q_l - S^{(0)}(s_l, t_l)$  be the difference vector between measured data and the corresponding points on the surface  $S^{(0)}$ , and take the initial adjusting matrix of the control points as

$$\Delta_{ij}^{(0)} = \mu_{ij} \sum_{l=1}^k B_i(s_l) B_j(t_l) \delta_l^{(0)}.$$

Then, add the adjusting matrix to the matrix of the control points  $[p_{ij}^{(0)}]$ . One obtains the new control points  $\mathbf{P}_{ij}^{(1)} = (s_i, t_j, p_{ij}^{(1)})$ , where  $p_{ij}^{(1)} = p_{ij}^{(0)} + \Delta_{ij}^{(0)}$ , which generates a new surface  $S^{(1)}$ . Hence, in the  $\beta$ th iteration, the  $\beta$ th surface is obtained. Then, one has

$$\begin{aligned} \delta_l^{(\beta)} &= q_l - S^{(\beta)}(s_l, t_l) \\ \Delta_{ij}^{(\beta)} &= \mu_{ij} \sum_{l=1}^k B_i(s_l) B_j(t_l) \delta_l^{(\beta)} \\ p_{ij}^{(\beta+1)} &= p_{ij}^{(\beta)} + \Delta_{ij}^{(\beta)} \end{aligned} \quad (6)$$

and  $(\beta + 1)$ st surface

$$S^{(\beta+1)}(s, t) = \sum_{i=0}^n \sum_{j=0}^n p_{ij}^{(\beta+1)} B_i(s) B_j(t) \quad s, t \in [0, 1].$$

The iteration will pause once the number of iterations is satisfied.

In the PB, let  $c_{i,j} = \sum_{l=1}^k B_i(s_l) B_j(t_l)$ , for  $i, j = 1, \dots, h$ , respectively, and  $C := \max_{1 \leq i, j \leq h} \{c_{i,j}\}$ . Note that  $C \neq 0$ . Then, one can take

$$\mu_{ij} = 1/C \quad (7)$$

that is, for different  $i$  and  $j$ , the weights  $\mu_{ij}$  are the same [29]. The algorithm 1 is given to compute the persistence grids. In the case that the initial values of  $z$ -coordinate of the control grid are set to be zero, LSPIA is proved to converge to the Moore-Penrose pseudo-inverse solution to the least-squares fitting result of the data set. And the time complexity of the algorithm is  $O(Nkh^2)$ , where  $N$  is the number of iterations,  $k$  is the number of points on a PD, and  $h$  is the density of control grid. [33] The convergence

and the computational complexity about LSPIA are attached in the Appendix B.

---

**Algorithm 1:** LSPIA for PB

---

**Input:** A measured data set  $\mathbf{Z} = \{(s_l, t_l, z_l)\}_{l=1}^k$ , a positive integer  $h$  representing the density of grid on  $[0, 1]^2$ , and a positive number  $N$  to represent the pause iterations

**Define** a function  $S^{(\beta)}(s, t) = \sum_{i=0}^h \sum_{j=0}^h \tilde{z}_{ij}^{(\beta)} B_i(s) B_j(t)$

$\mathbf{P}^{(0)} := [\tilde{z}_{ij}] = \mathbf{O}$ ;

Initiate  $\boldsymbol{\delta} = [\delta_l]$  and  $\boldsymbol{\Delta} = [\Delta_{ij}]$

**for**  $\beta = 0$ ;  $\beta \neq N$ ;  $\beta = \beta + 1$  **do**

$\delta_l^{(\beta)} = z_l - S^{(\beta)}(s_l, t_l)$ ;

$\Delta_{ij}^{(\beta)} = 2/C \sum_{l=1}^k B_i(s_l) B_j(t_l) \delta_l^{(\beta)}$ ;

$\tilde{z}_{ij}^{(\beta+1)} = \tilde{z}_{ij}^{(\beta)} + \Delta_{ij}^{(\beta)}$ ;

**end**

**Output:** the persistence vector  $\tilde{\mathbf{Z}}$  concatenated from each row of  $\mathbf{P}$

---

## 4 Stability

One of the most important properties of PDs is the stability with respect to tiny noise of the input data and errors resulting from measurements. In this section, it is shown that the vectors (3.2) generated by the control points of the persistence B-spline surface are stable with respect to the  $p$ -Wasserstein distance and the bottleneck distance between two PDs (definition 2.1).

In the very beginning, two lemmas are provided to support the following lemmas and theorems.

Lemma 4.1 is the fundamental theorem of calculus.

**Lemma 4.1.**  $f : \mathbb{R}^n \rightarrow \mathbb{R}$  is a  $C^1$ -continuous function on the closed interval  $H \subset \mathbb{R}^n$ , for any  $\mathbf{u}, \mathbf{v} \in H$ , we have

$$|f(\mathbf{u}) - f(\mathbf{v})| \leq \sup_{\tilde{\mathbf{u}} \in H} \|\nabla f(\tilde{\mathbf{u}})\|_2 \|\mathbf{u} - \mathbf{v}\|_2$$

In particular, if  $f : \mathbb{R} \rightarrow \mathbb{R}$ , then

$$|f(u) - f(v)| \leq \sup_{\tilde{u} \in H} |f'(\tilde{u})| |u - v|$$

*Proof.* It follows by the mean value theorem, the Cauchy-Schwarz inequality, and the extreme value theorem. Refer to [34].  $\square$

Lemma 4.2 gives the relationship of norms in a finitely dimensional space.

**Lemma 4.2.** For a finite-dimensional vector space  $\mathbb{R}^n$ , let  $\|\cdot\|_{p_1}$  and  $\|\cdot\|_{p_2}$  be given norms. Then there exist finite positive constants  $C_m$  and  $C_M$  such that  $C_m\|\mathbf{x}\|_{p_1} \leq \|\mathbf{x}\|_{p_2} \leq C_M\|\mathbf{x}\|_{p_1}$ , for any  $\mathbf{x} \in \mathbb{R}^n$ .

*Proof.* It follows immediately from Corollary 5.4.5 of Horn & Johnson [35].  $\square$

Here, some assumptions are made. Assume that each PD has a finite number of points  $\{(x_l, y_l)\}_1^k$  with persistences of its topological features being finite, i.e.,  $0 \leq y_l - x_l < \infty$  for each  $l$ , and  $k \leq \infty$ . In the PB, the eminence value  $z_l$  (8) is assigned to emphasize the importance of the points in a PD. Note that eminence function  $\mathcal{E}$  (8) is designed to be bounded. One obtains  $PD^{(1)}$  before a perturbation and the other  $PD^{(2)}$  after it.

First, we prove that the transformation from the birth-death coordinates to the birth-persistence coordinates is stable with respect to the  $p$ -Wasserstein distance and the bottleneck distance. There are the following two lemmas.

**Lemma 4.3.** For  $PD^{(1)}$  and  $PD^{(2)}$ ,  $b$  is the matching bijection which achieves the infimum in the  $p$ -Wasserstein distance or the bottleneck distance ( $p = \infty$ ). Let  $(x_l^{(2)}, y_l^{(2)}) = b((x_l^{(1)}, y_l^{(1)}))$ . Then, we have

$$\|\mathbf{Z}^{(2)} - \mathbf{Z}^{(1)}\|_p \leq C_{p,\mathcal{E}} W_p(PD^{(1)}, PD^{(2)}) \quad 1 \leq p \leq \infty$$

where  $\mathbf{Z}^{(1)}$  and  $\mathbf{Z}^{(2)}$  are the column vectors formed by  $z_l^{(1)}$  and  $z_l^{(2)}$ , respectively, and  $C_{p,\mathcal{E}}$  is a constant that depends on the eminence function  $\mathcal{E}$  and the  $p$ -norm.

*Proof.* Since  $|\mathcal{E}(x, y)| \leq M|f(y - x)|$ , it follows by using Lemma 4.1 that

$$|z_l^{(2)} - z_l^{(1)}| \leq M \sup |f'| \left| (y_l^{(2)} - x_l^{(2)}) - (y_l^{(1)} - x_l^{(1)}) \right|$$

where  $\sup |f'|$  denotes  $\sup_{\tilde{u} \in \mathbb{R}} |f'(\tilde{u})|$ .

For  $1 \leq p < \infty$ , we have

$$\|\mathbf{Z}^{(2)} - \mathbf{Z}^{(1)}\|_p \leq M \sup |f'| \left( \sum_l \left| y_l^{(2)} - x_l^{(2)} - y_l^{(1)} + x_l^{(1)} \right|^p \right)^{1/p}.$$

There is an inequation deduced by Lemma 4.2 that

$$|a - b| \leq |a| + |b| \leq 2 \max\{|a|, |b|\} \leq 2C_{\infty,p}(|a|^p + |b|^p)^{1/p}, \quad (8)$$

for all  $a, b \in \mathbb{R}$  and  $C_{\infty,p}$  is a constant that depends on  $p$ .

Then, we have

$$\|\mathbf{Z}^{(2)} - \mathbf{Z}^{(1)}\|_p \leq 2C_{\infty,p}M \sup |f'| \left( \sum_l |y_l^{(2)} - y_l^{(1)}|^p + |x_l^{(2)} - x_l^{(1)}|^p \right)^{1/p}.$$

$\mathbf{P}_l^{(1)}$  denotes  $(x_l^{(1)}, y_l^{(1)})$ , and  $b(\mathbf{P}_l^{(1)}) = (x_l^{(2)}, y_l^{(2)})$ . It follows by Lemma 4.2 that

$$\begin{aligned} \|\mathbf{Z}^{(2)} - \mathbf{Z}^{(1)}\|_p &\leq 2C_{\infty,p}M \sup |f'| \left( \sum_l \|\mathbf{P}_l^{(1)} - b(\mathbf{P}_l^{(1)})\|_p^p \right)^{1/p} \\ &\leq 2C_{\infty,p}C_{p,\infty}M \sup |f'| \left( \sum_l \|\mathbf{P}_l^{(1)} - b(\mathbf{P}_l^{(1)})\|_\infty^p \right)^{1/p} \\ &= C_{p,\varepsilon}W_p(PD^{(1)}, PD^{(2)}), \end{aligned}$$

where  $C_{p,\varepsilon} = 2C_{\infty,p}C_{p,\infty}M \sup |f'|$ .

For  $p = \infty$ , we have

$$\begin{aligned} \|\mathbf{Z}^{(2)} - \mathbf{Z}^{(1)}\|_\infty &\leq M \sup |f'| \max_l \left\{ |y_l^{(2)} - x_l^{(2)} - y_l^{(1)} + x_l^{(1)}| \right\} \\ &\leq 2M \sup |f'| \max_l \left( \max \left\{ |y_l^{(2)} - y_l^{(1)}|, |x_l^{(2)} - x_l^{(1)}| \right\} \right). \end{aligned}$$

Then, we immediately have

$$\begin{aligned} \|\mathbf{Z}^{(2)} - \mathbf{Z}^{(1)}\|_\infty &\leq 2M \sup |f'| \max_l \left\{ \|\mathbf{P}_l^{(1)} - b(\mathbf{P}_l^{(1)})\|_\infty \right\} \\ &\leq C_{\infty,\varepsilon}W_\infty(PD^{(1)}, PD^{(2)}). \end{aligned}$$

□

Lemma 4.3 shows that the  $z$ -coordinate after the transformation is stable. And then, the coordinates  $(s_l, t_l)$  (2) after the transformation are also stable given in Lemma 4.4.

**Lemma 4.4.** *For  $PD^{(1)}$  and  $PD^{(2)}$ , we have*

$$\|\mathbf{u} - \mathbf{v}\|_p \leq C_{p,m}W_p(PD^{(1)}, PD^{(2)}) \quad 1 \leq p \leq \infty$$

where

$$\begin{aligned} \mathbf{u} &= (s_1^{(1)}, \dots, s_k^{(1)}, t_1^{(1)}, \dots, t_k^{(1)}), \\ \mathbf{v} &= (s_1^{(2)}, \dots, s_k^{(2)}, t_1^{(2)}, \dots, t_k^{(2)}), \end{aligned}$$

and  $C_{p,m}$  is a constant that depends on  $m$  in (2) and the  $p$ -norm.

*Proof.* Recall the formula (1) in the paper that  $s_l = x_l/m$ ,  $t_l = (y_l - x_l)/m$ . For  $1 \leq p < \infty$ ,

$$\|\mathbf{u} - \mathbf{v}\|_p = \frac{1}{m} \left[ \sum_l |x_l^{(2)} - x_l^{(1)}|^p + |(y_l^{(2)} - x_l^{(2)}) - (y_l^{(1)} - x_l^{(1)})|^p \right]^{1/p}.$$

By using (8), we have

$$\begin{aligned} \|\mathbf{u} - \mathbf{v}\|_p &\leq \frac{1}{m} \left[ \sum_l |x_l^{(2)} - x_l^{(1)}|^p + 2^p C_{\infty,p}^p (|y_l^{(2)} - y_l^{(1)}|^p + |x_l^{(2)} - x_l^{(1)}|^p) \right]^{1/p} \\ &\leq \frac{1}{m} \left[ \sum_l (1 + 2^p C_{\infty,p}^p) (|y_l^{(2)} - y_l^{(1)}|^p + |x_l^{(2)} - x_l^{(1)}|^p) \right]^{1/p} \\ &= \frac{(1 + 2^p C_{\infty,p}^p)^{1/p}}{m} \left[ \sum_l \|\mathbf{P}_l^{(1)} - b(\mathbf{P}_l^{(1)})\|_p^p \right]^{1/p} \\ &\leq \frac{C_{p,\infty} (1 + 2^p C_{\infty,p}^p)^{1/p}}{m} \left[ \sum_l \|\mathbf{P}_l^{(1)} - b(\mathbf{P}_l^{(1)})\|_\infty^p \right]^{1/p} \\ &= C_{p,m} W_p(PD^{(1)}, PD^{(2)}), \end{aligned}$$

where  $C_{p,m} = (C_{p,\infty} (1 + 2^p C_{\infty,p}^p)^{1/p})/m$  is a constant that depends on  $m$  and the  $p$ -norm.

For  $p = \infty$ , we have a similar conclusion to Lemma 4.3:

$$\|\mathbf{u} - \mathbf{v}\|_\infty \leq C_{\infty,m} W_\infty(PD^{(1)}, PD^{(2)}).$$

□

Secondly, we will show the PB vector generated by the control grid of the B-spline surface approximating the data points  $(s_l, t_l, z_l)$  is stable w.r.t the  $W_p$  distance. Before that, the structures of B-spline basis matrix should be given, and the iterative format of LSPIA needs analyzing. The uniform cubic B-spline basis  $B_*(\cdot)$  ( $* = i, j$ ) are defined on uniform knot sequences

$$\xi_* = \left\{ 0, 0, 0, 0, \frac{1}{h-1}, \dots, \frac{h-2}{h-1}, 1, 1, 1, 1 \right\}, \quad (9)$$

for each  $i, j = 1, \dots, h$ . The explicit form of B-spline basis matrix  $\mathbf{B}$  is defined in equation (5). Each row of  $\mathbf{B}$  can be written as the row vectors  $[b_j(s, t)]$ :

$$\begin{aligned} b(s, t) &= [B_1(s)B_1(t), B_1(s)B_2(t), \dots, B_1(s)B_h(t), \\ &\quad B_2(s)B_1(t), B_2(s)B_2(t), \dots, B_2(s)B_h(t), \dots, \\ &\quad B_h(s)B_1(t), B_h(s)B_2(t), \dots, B_h(s)B_h(t)] \\ &:= [B_1(s, t), B_2(s, t), \dots, B_r(s, t)] \end{aligned}$$

$$\mathbf{B} = \begin{bmatrix} B_1(\cdot_1) & B_2(\cdot_1) & B_3(\cdot_1) & \cdots & B_r(\cdot_1) \\ B_1(\cdot_2) & B_2(\cdot_2) & B_3(\cdot_2) & \cdots & B_r(\cdot_2) \\ \vdots & \vdots & \vdots & \cdots & \vdots \\ \vdots & \vdots & \vdots & \cdots & \vdots \\ B_1(\cdot_k) & B_2(\cdot_k) & B_3(\cdot_k) & \cdots & B_r(\cdot_k) \end{bmatrix} \quad (10)$$

where  $(\cdot_j)$  denotes  $(s_j, t_j)$ ,  $j = 1, 2, \dots, k$  and  $r = h^2$ .

The iterative format (6) is rewritten in matrix form,

$$\begin{aligned} \tilde{\mathbf{Z}}^{(\beta+1)} &= \tilde{\mathbf{Z}}^{(\beta)} + \Lambda \mathbf{B}^T (\mathbf{Z} - \mathbf{B} \tilde{\mathbf{Z}}^{(\beta)}) \\ \tilde{\mathbf{Z}}^{(0)} &= \mathbf{O}, \end{aligned} \quad (11)$$

where  $\Lambda = \text{diag}(1/C, 1/C \cdots, 1/C)$  is a diagonal matrix, and  $\mathbf{B}$  is the B-spline basis matrix shown above.

Next, the stability of the persistence vectors computed by LSPIA method is discussed. According to the iterative format (11), there is an equivalent form

$$\tilde{\mathbf{Z}}^{(\beta+1)} = (\mathbf{E} - \Lambda \mathbf{B}^T \mathbf{B}) \tilde{\mathbf{Z}}^{(\beta)} + \Lambda \mathbf{B}^T \mathbf{Z}, \quad (12)$$

The iteration is run for a finite number  $N$  to compute the persistence grids. Hence, one has

$$\tilde{\mathbf{Z}}^{(N)} = \left[ \sum_{i=0}^{N-1} (\mathbf{E} - \Lambda \mathbf{B}^T \mathbf{B})^i \right] \Lambda \mathbf{B}^T \mathbf{Z}, \quad (13)$$

where  $\mathbf{E}$  is identity matrix. Let  $\bar{\mathbf{B}}$  be  $\left[ \sum_{i=0}^{N-1} (\mathbf{E} - \Lambda \mathbf{B}^T \mathbf{B})^i \right] \Lambda \mathbf{B}^T$ , and equation (13) can be rewritten to be

$$\tilde{\mathbf{Z}}^{(N)} = \bar{\mathbf{B}} \mathbf{Z}. \quad (14)$$

Then, we discuss the case when  $N$  is finite. And the case when  $N$  approaches to infinity is also discussed with an assumption about the data set in Appendix C. Here, we give a lemma about the continuity of each entry as a function of the matrix  $\bar{\mathbf{B}}$ .

**Lemma 4.5.** *Every entry of the matrix  $\bar{\mathbf{B}}$  is a continuous and piecewise- $C^1$  rational function of the variables  $s_1, t_1, \dots, s_k, t_k$  on the closed interval  $[0, 1]^{2k}$ .*

*Proof.* Each entry  $\bar{b}_{ij}$  of the matrix  $\bar{\mathbf{B}}$  may be seen as a function whose variables are  $s_1, t_1, \dots, s_k, t_k$ , and its domain is  $[0, 1]^{2k}$ . Recall that

$$\Lambda = \text{diag}(1/C, 1/C \cdots, 1/C),$$

where  $C = \max_{1 \leq i, j \leq h} \left\{ \sum_{l=1}^k B_i(s_l) B_j(t_l) \right\} \neq 0$ . Since each entry in  $\mathbf{B}$  and  $\mathbf{\Lambda}$  is a continuous and piecewise- $C^1$  rational function of the variables  $s_1, t_1, \dots, s_k, t_k$ , i.e., it can be written as a quotient of polynomials on the closed interval  $[0, 1]^{2k}$ . Note that it is still a continuous and piecewise- $C^1$  rational function after a finite number of additions and multiplications. Hence, every entry of the matrix  $\bar{\mathbf{B}}$  is a continuous and piecewise- $C^1$  rational function on the closed interval  $[0, 1]^{2k}$ .  $\square$

Finally, for the results of the transformed coordinates and the continuity of the iterative matrix, the stability of the persistence vectors generated by the control points of the persistence B-spline surface is obtained.

**Theorem 4.1** (Stability). *For  $PD^{(1)}$  and  $PD^{(2)}$ , their  $p$ -Wasserstein distance ( $1 \leq p \leq \infty$ ,  $p = \infty$  means the bottleneck distance) is given by  $W_p(PD^{(1)}, PD^{(2)})$ .*

We have

$$\|\tilde{\mathbf{Z}}^{(2)} - \tilde{\mathbf{Z}}^{(1)}\|_p \leq C_{p,m,N,\mathcal{E}} W_p(PD^{(1)}, PD^{(2)}) \quad 1 \leq p \leq \infty,$$

where  $\tilde{\mathbf{Z}}^{(1)}$  and  $\tilde{\mathbf{Z}}^{(2)}$  are the persistence vectors generated by  $PD^{(1)}$  and  $PD^{(2)}$ , respectively.  $C_{p,m,N,\mathcal{E}}$  is a constant that depends on the  $p$ -norm, the transformation (2), the iterations  $N$  of LSPIA, and the eminence function (8).

*Proof.*  $\bar{\mathbf{B}}^{(1)}$  and  $\bar{\mathbf{B}}^{(2)}$  are the matrices in LSPIA with a finite number of iterations  $N$  determined by  $PD^{(1)}$  and  $PD^{(2)}$ , respectively. It follows by Lemma 4.5 that each entry  $\bar{b}_{ij}$  has a extremum, a finite positive number  $M_{ij} \in \mathbb{R}$  on  $[0, 1]^{2k}$ , such that  $|\bar{b}_{ij}(s_1, t_1, \dots, s_k, t_k)| \leq M_{ij}$ .

Then, it is defined  $\|\cdot\|_2$  to be a vector norm on matrices given in Definition 5.6.1 of [35]. For each row  $[\bar{b}_{i*}]$  of  $\bar{\mathbf{B}}$ ,  $i = 1, \dots, k$ ,

$$|[\bar{b}_{i*}] \cdot \mathbf{x}| \leq \|[\bar{b}_{i*}]\|_2 \|\mathbf{x}\|_2,$$

for any  $\mathbf{x} = [x_j]$  satisfying  $\|\mathbf{x}\|_2 = 1$ .

We have

$$\|\bar{\mathbf{B}}\mathbf{x}\|_2 \leq \left( \sum_{ij} b_{ij}^2 \right)^{1/2} \leq \left( \sum_{ij} M_{ij}^2 \right)^{1/2} := M_1.$$

Consequently,  $\|\bar{\mathbf{B}}\|_2 \leq M_1$  for both  $PD^{(1)}$  and  $PD^{(2)}$ , where  $M_1$  depends on the iteration  $N$  in LSPIA.

Then, it follows by the property of the vector norm on matrices (Theorem 5.6.2 (b) of [35]) that

$$\|(\bar{\mathbf{B}}^{(2)} - \bar{\mathbf{B}}^{(1)})\mathbf{Z}\|_2 \leq \|\bar{\mathbf{B}}^{(2)} - \bar{\mathbf{B}}^{(1)}\|_2 \|\mathbf{Z}\|_2.$$

Let  $\mathbf{u}$  and  $\mathbf{v}$  denote  $(s_1^{(1)}, t_1^{(1)}, \dots, s_k^{(1)}, t_k^{(1)})$  and  $(s_1^{(2)}, t_1^{(2)}, \dots, s_k^{(2)}, t_k^{(2)})$ , respectively. It follows by Lemma 4.1 and Lemma 4.5 that, for each entry of  $\bar{\mathbf{B}}$ ,

$$|b_{ij}(\mathbf{u}) - b_{ij}(\mathbf{v})| \leq \sup_{\tilde{\mathbf{u}} \in H} \|\nabla b_{ij}(\tilde{\mathbf{u}})\|_2 \|\mathbf{u} - \mathbf{v}\|_2.$$

And we have

$$\|\bar{\mathbf{B}}^{(2)} - \bar{\mathbf{B}}^{(1)}\|_2 \leq M_2 \|\mathbf{u} - \mathbf{v}\|_2,$$

where  $M_2 = \left[ \sum_{ij} (\sup_{\tilde{\mathbf{u}} \in H} \|\nabla b_{ij}(\tilde{\mathbf{u}})\|_2)^2 \right]^{1/2} < \infty$  is a constant that depends on the iteration  $N$ .

Eventually, let  $W_p$  denote  $W_p(PD^{(1)}, PD^{(2)})$ . For  $1 \leq p \leq \infty$ , we have

$$\begin{aligned} \|\tilde{\mathbf{Z}}^{(2)} - \tilde{\mathbf{Z}}^{(1)}\|_p &\leq C_{p,2} \|\bar{\mathbf{B}}^{(2)} \mathbf{Z}^{(2)} - \bar{\mathbf{B}}^{(1)} \mathbf{Z}^{(1)}\|_2 \\ &= C_{p,2} \|\bar{\mathbf{B}}^{(2)} \mathbf{Z}^{(2)} - \bar{\mathbf{B}}^{(2)} \mathbf{Z}^{(1)} + \bar{\mathbf{B}}^{(2)} \mathbf{Z}^{(1)} - \bar{\mathbf{B}}^{(1)} \mathbf{Z}^{(1)}\|_2 \\ &\leq C_{p,2} (\|\bar{\mathbf{B}}^{(2)} (\mathbf{Z}^{(2)} - \mathbf{Z}^{(1)})\|_2 + \|(\bar{\mathbf{B}}^{(2)} - \bar{\mathbf{B}}^{(1)}) \mathbf{Z}^{(1)}\|_2) \\ &\leq C_{p,2} (\|\bar{\mathbf{B}}^{(2)}\|_2 \|\mathbf{Z}^{(2)} - \mathbf{Z}^{(1)}\|_2 \\ &\quad + \|(\bar{\mathbf{B}}^{(2)} - \bar{\mathbf{B}}^{(1)})\|_2 \|\mathbf{Z}^{(1)}\|_2) \\ &\leq C_{p,2} (M_1 \|\mathbf{Z}^{(2)} - \mathbf{Z}^{(1)}\|_2 + M_2 \|\mathbf{u} - \mathbf{v}\|_2 \|\mathbf{Z}^{(1)}\|_2) \\ &\leq C_{p,2} C_{2,p} (M_1 C_{p,\mathcal{E}} + M_2 C_{p,m} \|\mathbf{Z}^{(1)}\|_2) W_p \\ &\leq C_{p,2} C_{2,p} (M_1 C_{p,\mathcal{E}} + M_2 C_{p,m} C_{2,\infty} \|\mathbf{Z}^{(1)}\|_\infty) W_p \\ &\leq C_{p,2} C_{2,p} (M_1 C_{p,\mathcal{E}} + M_2 C_{p,m} C_{2,\infty} \sup |\mathcal{E}|) W_p \\ &= C_{p,m,N,\mathcal{E}} W_p(PD^{(1)}, PD^{(2)}), \end{aligned}$$

where  $C_{p,m,N,\mathcal{E}}$  denotes  $C_{p,2} C_{2,p} (M_1 C_{p,M,|p'|} + M_2 C_{p,m} C_{p,m} C_{2,\infty} \sup |\mathcal{E}|)$ , which is a constant that depends on the  $p$ -norm, the transformation  $c \circ \phi$ , the iteration  $N$  in LSPIA, and the eminence function  $\mathcal{E}$ .  $\square$

Note that the form of the stable coefficient  $C_{p,m,N,\mathcal{E}}$  given in Theorem 4.1 does not explicitly show the relationship between the coefficient and the variables, especially the the number of iterations  $N$ . Therefore, an experiment in Appendix D was designed to attempt to make it clear.

## 5 Experiments

In this section, evaluation of PB, and performance comparison of PB and other vectorizing representations are exhibited. In all experiments, the  $H_0$  and  $H_1$  PDs were computed by constructing the V-R filtration on each point cloud in the sense of Euclidean

metric on  $\mathbb{R}^2$  or  $\mathbb{R}^3$ . The technique of the reduced homology was used to avoid the topological feature with infinite persistence occurring in  $H_0$  PDs. All experiments were run on a PC with Inter(R) Core(TM) i7-7700 CPU@3.60GHz×8. Datasets and the MATLAB and Python code can be found on <https://github.com/ZC119/PB>.

## 5.1 Evaluation of PB

To evaluate PB, the choice of the parameters of the PB algorithm by the task of classification on a relatively simple synthetic data set sampled from five models in a normal 2D square is discussed. And tests about the features PB can extract from a PD on a randomly generated PDs are given.

### 5.1.1 Parameter Choice

The algorithm was tested for a task of classification on a simple synthetic toy data set that contained a circle with its radius 0.4, two concentric circles with their radii 0.2 and 0.4, respectively, two disjoint circles with both their radii 0.2, a cluster of points sampled at random in the normal square, and two clusters of points sampled at random separately in two squares with edge length 0.5. All data were sampled in the range of  $[-0.5, 0.5]^2$  on the 2D plane. Each sampling formed an image (Figure 9). Then, 50 images were obtained for each kind, and 1000 points were sampled for each image. In the tests, the sampled data were perturbed by adding Gaussian noises ( $\eta = 0.025$ ) onto each image.

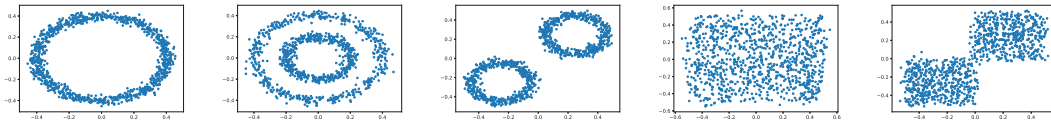


Figure 3: The sampling points from five classes of the toy data. Each sampling is perturbed by a Gaussian noise with  $\eta = 0.025$ .

In practice, PB relies on the iteration of LSPIA, the density of underlying control grid, and the eminence function that indicate the importance of each point in a PD. The iteration was increased from 100 to 1000 with the increment 100 in the uniform control grid of  $20 \times 20$ . The vectors were computed in the different density of uniform control grid from a sparse grid ( $15 \times 15$ ) to a dense one ( $100 \times 100$ ) with the increment 5 in every coordinate. In both tests, the LSPIA was iterated for 100 times. The eminence

Table 1: Classification accuracy under  $20 \times 20$  control grid (for  $H_0$ , a uniform B-spline curve with 20 control points was used) and average classification accuracy of different density of uniform control grids ranging from 15 to 100 with the increment 5.

Classifier	$H_0$	$H_0$	$H_1$	$H_1$
	Average Accuracy	$20 \times 1$ Accuracy	Average Accuracy	$20 \times 20$ Accuracy
RF	93.6%	97.4%	99.7%	99.8%
GBDT	94.9%	97.3%	98.5%	98.7%
LR	91.3%	91.0%	97.8%	100%
LSVM	91.7%	94.8%	99.5%	100%

function was considered in different tasks and left to be decided by users. In this task,  $\varepsilon = 10^{-3}$  was taken for computing the vectors from  $H_0$  PDs,  $\varepsilon = 10^{-10}$  for  $H_1$  PDs and the bound constant  $M = 10$ .<sup>2</sup>

The following four classifiers were used: random forest (RF) [36], gradient boosted decision trees (GBDT) [37], logistic regression (LR) and linear support vector machine (LSVM) [38]. They are powerful algorithms for supervised learning. RF and GBDT are ensemble learning algorithms that train multiple weak learners to obtain better classification performance. RF is a classifier that fits many decision trees on different subsets of data and then uses averaging to overcome overfitting. GBDT is one of the boosting algorithms combining weak learners with a strong learner iteratively. Logistic regression is applied for multiclass classification using the one-vs.-rest (OvR) scheme and LSVM using one-vs.-rest similarly. For PDs, a package for Python, Ripser.py [39], was used. For each classifier, data were split into 70% training set and 30% test set, 100 trials were performed, and the average classification accuracy was computed.

As shown in Figure 10, in this task, PB is relatively insensitive to the iteration of LSPIA and the density of the control grid, although a slight decrease of the accuracy occurs under the classifier LR with the density of the control grid increases (shown by blue dashed line in the left figure of Figure 10). Meanwhile, it is observed in Table 1 that the PB representation made it possible to capture the topological feature of the data accurately, and all of the classifiers reached high accuracies on PB ( $H_1$   $20 \times 20$ ).

<sup>2</sup> For the eminence function  $\mathcal{E}(x, y)$  (8),  $L = m$  in (3) was taken, and  $M$  equaled the maximum of the numbers of points of PDs. The parameter  $\varepsilon$  in (8) was selected in different tasks.

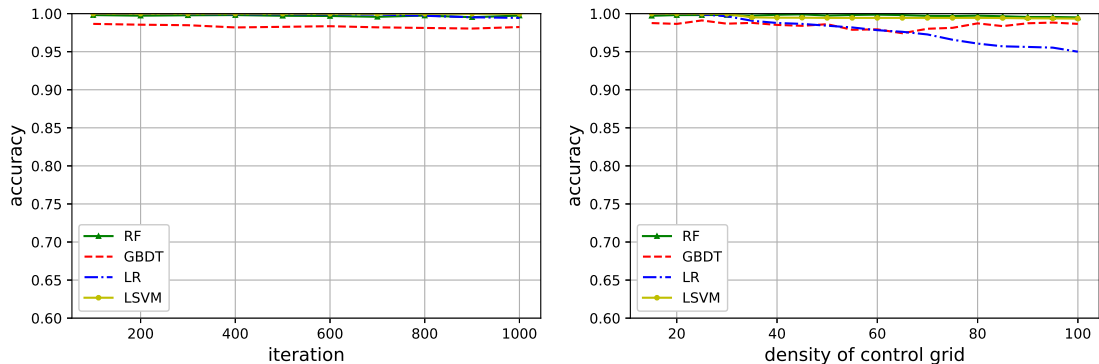


Figure 4: Classification accuracy of four methods with the increasing of iteration of LSPIA and density of control grid according to the  $H_1$  features. Left figure: the iteration is increased from 100 to 1000 with the increment 100 in the uniform control grid of  $20 \times 20$ . Right figure: the density of uniform control grid is increased from a sparse grid ( $15 \times 15$ ) to a dense one ( $100 \times 100$ ) with the increment 5 in every coordinate.

### 5.1.2 Classification of Randomly Generated PDs

To evaluate PB and eliminate over-performance of PB, randomly generated PDs were classified. This exercise attempts to illustrate what PD features PB can catch, and to clarify whether PB denoises PDs and emphasizes some inapparent features on PDs to over-perform. We referred to the approach of generating random PDs in [12], where the authors used randomly generated PDs to verify their method of calculating the distance between two PDs. In their tests, a random PD was partially produced in the following manner. The points are located above the diagonal with non-negative birth coordinates, and are of the form  $(x - \tau|y|/2, x + \tau|y|/2)$ , where  $x$  is drawn uniformly in  $[0, 1]$ ,  $\tau$  is a positive constant, and  $y$  is chosen from a normal distribution  $N(0, 1)$ . Additionally, a valid point on a PD must satisfy  $0 \leq x - \tau|y|/2 \leq x + \tau|y|/2 \leq 1$ . PDs generated in this manner are comparable with actual PDs on which most of points concentrate closely to the diagonal.

**Extracted Features via PB:** To clarify what can be extracted from a PD by PB method and which features of PD cannot be captured via PB, we performed two tests on designed randomly generated PDs. In the first test, five categories of synthetic random PDs were designed, with each category having some points with relatively long persistence to mark the difference of the category. The details are as follows. Let  $\mathbf{P}_1 =$

$(0.1, 0.8)$ ,  $\mathbf{P}_2 = (0.3, 0.7)$ ,  $\mathbf{P}_3 = (0.7, 0.9)$ , and  $PD_r$  denote the random PD mentioned. For the test, we set  $\tau = 0.02$  and the number of points close to the diagonal equal to 50.  $\bar{\mathbf{P}}_i$  denotes the point  $\mathbf{P}_i$  with a small perturbation, where  $i = 1, 2, 3$ . PDs in five categories were produced by  $PD_r$ ,  $PD_r \cup \bar{\mathbf{P}}_1$ ,  $PD_r \cup \bar{\mathbf{P}}_2$ ,  $PD_r \cup \bar{\mathbf{P}}_3$ , and  $PD_r \cup \bar{\mathbf{P}}_2 \cup \bar{\mathbf{P}}_3$ ; 20 PDs were produced in each category. We computed PB vectors with the following parameters: LSPIA iteration  $N = 100$ , grid size  $20 \times 20$ ,  $\varepsilon = 0, 0.01, 0.02, 0.05$ . The classifier of  $k$ -nearest neighbors ( $k$ NN) was employed in this classification task. In Table 2, classification accuracies are listed for five classifiers ( $k$ NN, RF, GBDT, LR, and LSVM) with their hyperparameters defaulted.

Table 2: Classification accuracy of designed random PDs with different points having long persistence through five classifiers ( $k$ NN, RF, GBDT, LR, and LSVM): the PB vectors are generated with iteration  $N = 100$ , and  $\varepsilon = 0, 0.01, 0.02, 0.05$  in eminence function, respectively.

Accuracy (%)	$\varepsilon = 0.00$	$\varepsilon = 0.01$	$\varepsilon = 0.02$	$\varepsilon = 0.05$
$k$ NN	99.8%	99.7%	99.3%	82.0%
RF	99.0%	96.7%	97.6%	97.3%
GBDT	91.7%	93.0%	93.7%	92.3%
LR	99.7%	99.7%	99.5%	94.0%
LSVM	100%	100%	100%	97.7%

As shown in Table 2, the values of classification accuracy are relatively large, which implies that PB can catch those single points with long persistence and that PB vectors can be distinguished on all classifiers. Interestingly, the classification accuracy decreases slightly as the parameter  $\varepsilon$  increases. A larger  $\varepsilon$  implies that more points are probably considered in an  $\varepsilon$ -neighborhood of a certain point on a PD. With this test, we could also consider the local density of points that traditional PD measurements, i.e., the  $p$ -Wasserstein distance and the bottleneck distance, do not consider. By setting  $\varepsilon = 0$ , the local density is not considered. The slight decline of classification accuracy as  $\varepsilon$  increases could be because a large  $\varepsilon$  might emphasize the points densely scattered above the diagonal by enlarging their eminence values.

In the second test, we assumed that there are different numbers of points, close to each other, with long persistence in a PD. Similarly, five categories of PDs were designed: a PD in  $i$ th category is a union of a random PD and  $i$  perturbed  $\bar{\mathbf{P}}_1$ 's, where  $i = 1, 2, \dots, 5$ . When producing PDs, the parameter  $\tau$  in random PDs is set to 0.02, and the number of points above the diagonal is set to 50. 20 PDs were produced in each

category. Similar to the previous test, we computed PB vectors with  $\varepsilon = 0, 0.01, 0.05, 0.1$  in eminence function and we defaulted the hyperparameters of five classifiers ( $k$ NN, RF, GBDT, LR, and LSVM) . Classification accuracies for the second test are listed in Table 3. It is found that PB cannot catch points that are too close to each other on a PD, unless the local density is considered. In fact, the PB surface is a surface that approximates the points with their coordinates; the coordinates, in turn, are obtained from the birth–death coordinates and the eminence value, orderly. If several points are quite close to each other, the PB surface cannot capture their difference if the size of the control grid is fixed. Considering the local density, it is possible to note that as the parameter  $\varepsilon$  increases, more density information is considered, and the classification accuracies improve prominently in some classifiers, such as  $k$ NN. A reasonable explanation for this improvement is that the eminence values of points with long persistence increase as the number of points increases, which causes a recognizable difference of distances between PB vectors in two different categories.

Table 3: Classification accuracy of designed random PDs with different numbers of points having long persistence through five classifiers ( $k$ NN, RF, GBDT, LR, and LSVM): the parameter  $\varepsilon$  in eminence function is set to be 0, 0.01, 0.05, 0.10, respectively.

Accuracy (%)	$\varepsilon = 0.00$	$\varepsilon = 0.01$	$\varepsilon = 0.05$	$\varepsilon = 0.10$
$k$ NN	30.3%	45.3%	92.7%	97.0%
RF	26.0%	39.0%	46.3%	50.7%
GBDT	29.0%	34.7%	86.0%	90.0%
LR	23.7%	44.0%	58.7%	58.7%
LSVM	26.7%	44.0%	58.3%	55.7%

In summary, PB can capture topological features with long persistence, while it is insensitive to points closely packed together. A denser control grid of B-spline surface would overcome this insensitivity problem; however, it will also improve the dimension of the PB vector. As a result, it is important to appropriately consider the local density of points in an  $\varepsilon$ -neighborhood when the eminence value of each point on a PD is assigned. The experiment shows that involving local density points results in a positive effect, and it also implies the parameter  $\varepsilon$  should be selected carefully via tests of parameter selection.

**Elimination of Over-performance:** To test whether the results of classification using PB are not random, namely the method reducing noise in a sense to improve

the performance, the task to classify a set of randomly generated PDs was designed. When generating random PDs, the number of points each synthetic PD contains was produced by rounding a positive number satisfying a normal distribution  $N(200, 10)$ . We set the parameter  $\tau = 1$  and we generated 100 PDs. Finally, PB vectors with different parameters (set iteration  $N = 100$  fixed, grid size  $20 \times 20$ ,  $\varepsilon = 0, 0.01, 0.05, 0.10$  in eminence function, respectively) were computed. Figure 5 provides an example of randomly generated PD. We chose default parameters for the hyperparameters of each classifier ( $k$ NN, RF, GBDT, LR and LSVM). We performed 50 tests, where the PDs were randomly yet uniformly separated into five classes (20 PDs per class). In each test, the data set was randomly split into 70% – 30% training and test sets, which was repeated 100 times to obtain the average of classification accuracy for each classifier.

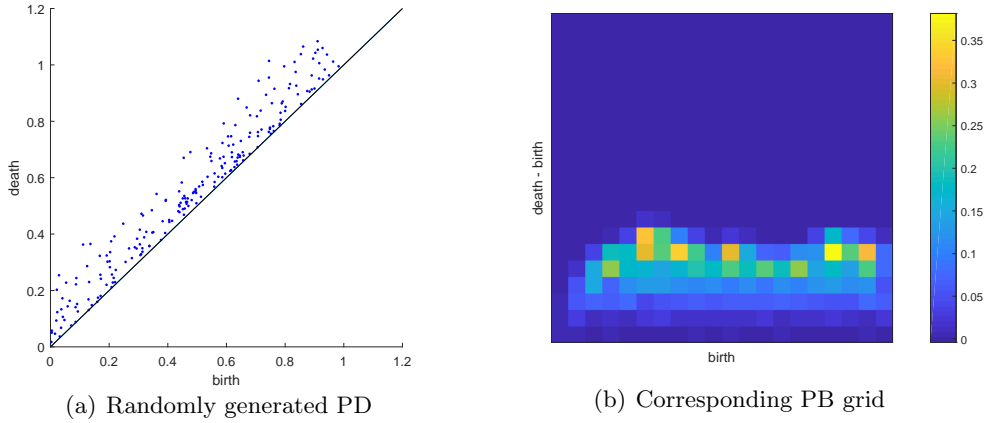


Figure 5: Randomly generated PD and its PB grid: A randomly generated PD with 212 points above the diagonal is shown in (a); the PB grid with persistence values as values of eminence and its size  $20 \times 20$  is shown in (b).

The average accuracy of all tests on every classifier is listed in table 4. Overall, the accuracy is close to that of a random guess (about 20%) and the variance of accuracy is relatively small. This result suggests that the PB method fails to emphasize some noticeable features on PDs to perform better in all classifiers. In other words, the PB method does not reduce the noise present in. It is because the points close to the diagonal also contribute to the evaluation of some entries of control grid. Intuitively, the persistence B-spline surface is smooth, yet it does not imply that the tiny features on a PD are diminished during the process of computing the corresponding PB vector.

Table 4: Classification accuracy of randomly generated PDs through five classifiers ( $k$ NN, RF, GBDT, LR, and LSVM): the PB vectors are generated with iteration  $N = 100$  fixed, and  $\varepsilon = 0, 0.01, 0.05, 0.1$  in eminence function, respectively.

Accuracy (%)	$\varepsilon = 0.00$	$\varepsilon = 0.01$	$\varepsilon = 0.05$	$\varepsilon = 0.10$
$k$ NN	20.2±0.4%	21.8±0.7%	21.0±0.4%	19.3±0.5%
RF	19.0±0.7%	19.3±0.2%	20.3±0.2%	20.0±0.2%
GBDT	19.3±0.3%	18.3±0.5%	20.7±0.7%	19.7±0.3%
LR	20.2±0.2%	20.5±0.8%	19.0±0.7%	19.6±0.2%
LSVM	19.7±0.2%	20.1±0.6%	18.9±0.7%	19.1±0.2%

## 5.2 Classification Experiments

To compare with other methods including nonlearnable methods (distance matrix of  $W_p$  distance, PI, PL) and kernel methods (PSSK, PWGK, SWK), The experiments were done on data generated from a discrete dynamical system models and a 3D CAD model dataset. The performances of these methods in the task of classification were compared.

### 5.2.1 Classification of Parameters of a 3D Dynamical System

Dynamical system models can simulate some natural phenomena. To make the model approximate to the reality, several parameters in a dynamical system have to be determined. PD provides a visual tool for representing the potential topological features in dynamical data. Adams et al. [23] offer an application of parameter determination of the linked twist map [40], a 2D dynamical model. In this experiment, PLs, PIs, PBs and PDs were tested in a 3D dynamical system to observe their performances when classifying a more complicated dataset.

The dynamical system proposed by Lindström [41] describes a discrete food chain model defined by

$$\begin{aligned} X_{t+1} &= \frac{M_0 X_t \exp(-Y_t)}{1 + X_t \max\{\exp(-Y_t), K(Z_t)K(Y_t)\}} \\ Y_{t+1} &= M_1 X_t Y_t \exp(-Z_t) K(Y_t) \cdot K(M_3 Y_t Z_t) \\ Z_{t+1} &= M_2 Y_t Z_t \end{aligned}$$

where

$$K(x) = \begin{cases} \frac{1 - \exp(-x)}{x}, & x \neq 0 \\ 1 & x = 0 \end{cases}$$

Table 5: Time cost (seconds) from inputting PDs to generating distance matrices for direct computation of 1-Wasserstein distance, 2-Wasserstein distance, and the bottleneck distance (PDs,  $L_1$ ; PD,  $L_2$ ; PD,  $L_\infty$ ), PLs, PIs, and PBs.

<b>Time (s)</b>	$H_1, L_1$	$H_1, L_2$	$H_1, L_\infty$
PD	667s	1251s	983s
PL	32s	48s	<b>6s</b>
PI	<b>10s</b>	<b>10s</b>	10s
PB	<b>10s</b>	<b>10s</b>	10s

Table 6: Classification accuracies of  $k$ NN for direct computation of 1-Wasserstein distance, 2-Wasserstein distance, and the bottleneck distance (PD,  $L_1$ ; PD,  $L_2$ ; PD,  $L_\infty$ ), PLs, PIs and PBs.

<b>Accuracy</b>	$H_1, L_1$	$H_1, L_2$	$H_1, L_\infty$
PD	78.8±0.6%	76.8±0.6%	71.9±0.7%
PL	75.7±0.7%	73.4±0.6%	71.5±0.7%
PI	78.6±0.5%	80.9±0.6%	78.9±0.8%
PB	<b>82.8±0.4%</b>	<b>82.6±0.3%</b>	<b>81.0±0.3%</b>

The variables  $X, Y$  and  $Z$  are related to the trophic levels of the food chain system.  $X$  and  $Z$  are proportional to vegetation abundance and carnivore abundance, respectively, and  $Y$  has a nonlinear and complicated relation to herbivore abundance. Osipenko [42] studied the attractor of the system with fixed parameters  $M_1 = 1.0, M_2 = M_3 = 4.0$  and variable parameter  $M_0 \in [3.00, 3.65]$ . Referring to Chapter 17 of [42],

$$M_0 = 3.0, 3.3, 3.48, 3.54, 3.57, 3.532, 3.571, 3.3701, 3.4001$$

were taken, respectively, and nine classes of results were obtained with various parameters  $M_0$ . For each class, the initial values  $(X_0, Y_0, Z_0)$  were generated randomly in the region  $(1, 2) \times (0, 1)^2$ , and the system was iterated 2000 times to obtain the points in the 3D Euclidean space. Each combination of parameters was repeated 50 times, and eventually 450 results were obtained from the system. This experiment was done to compare the classification effects among the methods of PLs, PIs, PBs, and PDs.

In the comparison, the software [12] was used to compute the Wasserstein distances and the bottleneck distance. For PLs, the Persistence Landscapes Toolbox [19] was used. For PIs, the open-source MATLAB codes [23] were used. The PIs were computed

Table 7: Classification performances for  $H_1$  PDs in five classifying approaches: PIs ( $20 \times 20$ ,  $\sigma = 10^{-3}$ ), PBs ( $20 \times 20$ ,  $\varepsilon = 10^{-1}$ ), kernel methods (SWK, PWGK, PSSK) were computed.

Accuracy (%)	$k$ NN	RF	GBDT	LR	LSVM
PB	82.6±0.3%	83.2±0.7%	82.8±0.7%	84.8±0.5%	<b>86.8±0.5%</b>
PI	80.9±0.6%	79.0±0.6%	78.8±0.4%	67.8±0.6%	73.4±0.5%
Accuracy(%)	Kernel SVM				
SWK	<b>87.2±0.3%</b>				
PWGK	80.9±0.5%				
PSSK	78.2±0.6%				

with their resolutions  $20 \times 20$ , and the  $\sigma = 10^{-3}$  in PIs were adjusted to guarantee the best result. In PBs,  $\varepsilon = 10^{-1}$  was taken in the eminence function (8), and a  $20 \times 20$  uniform control point grid was used.  $k$ NN is a simple classification algorithm in which the distance metric on the space can be used. Distance matrices were created according to  $L_1$ ,  $L_2$ , or  $L_\infty$  distances.<sup>3</sup> Then,  $k$ NN was used to classify the data by using the distance matrices. Here,  $k = 3$  was set, and data were split randomly into a 70% training set and a 30% test set. The classification was performed 10 times, in each of which 100 trials were done and the average classification accuracy was computed. As Table 5 and Table 6 show, in the case of low density of the control grid in PB, PB is almost as efficient as PI in this task. PB performs nicely under the  $k$ NN classifier with respect to  $L_1$ ,  $L_2$  and  $L_\infty$  norms of the vector spaces.

Meanwhile, the PB was also tested under various classifiers (RF, GB, LR and LSVM) and compared with PI and kernel methods (SWK, PWGK, and PSSK) on SVM. After the cross validation, the hyperparameter  $C$  of SVM was adjusted to 10 for all kernel methods, and in PWGK, the parameters  $K$  and  $\rho$  were selected to be 100 and 0.01, respectively. It is observed that PB and SWK perform better than other methods (see Table 7) in this more complicated task of classifying nine collections of this 3D dynamical system with different parameters. Inevitably, the parameters of PB (the eminence function) in the experiment were selected, but the choice of parameters cost little time ( $\varepsilon = 10^{-1}$ ,  $10^{-2}$ , and  $10^{-3}$  was picked).

<sup>3</sup> For PDs, they are  $W_1$ ,  $W_2$  and  $W_\infty$  distances. For vector representations, they are 1, 2,  $\infty$ -norms of the vector space. —

## 5.2.2 Classification of 3D CAD Models

Point cloud in space is a universal representations to model a geometric object. While the topology of point clouds plays an important role in the classification of a point cloud dataset, it is seemingly impossible to classify most objects through topology only, especially with shapes of similar topology. However, it is a reliable alternative to distinguish shapes with topological differences. The PD of a point cloud is likely to contain crucial information that helps classify 3D shapes.

We tested our method on a subcategory of the ModelNet40 [43], a shape classification benchmark usually employed by deep neural network to evaluate the network models. The benchmark includes 12,311 CAD models classified into 40 object categories. Compared with approaches based on deep neural networks, the classification accuracy of PB on the full benchmark is approximately 35% on GBDT classifier and approximately 28% on SVM classifier to classify shapes from 40 object categories, because the semantics of 3D shapes is considered in the man-made categories so that the non-learnable method can hardly recognized the category of an object by only using topological features. For example, the four categories “bottle, “bowl, “cup, “flowerpot, significantly different in the man-made categorization, have nearly the same geometric and topological structure. The performance of PB vectors for classifying these four categories was almost a random guess (about 27%). Thus, we selected seven categories with 1970 models in total to evaluate the PB and other methods. The categories selection was based taking into account the (1) difference of topology, and the (2) interference of shape semantics. More details on this process are given in Appendix E. For the experiment, the dataset was randomly split into 70%-30% training and test set. All experiments were repeated 100 times to obtain the averages.

PB and PI were tested on the five classifiers  $k$ NN, RF, GBDT, LR, and linear SVM. The hyperparameters of the first four classifiers were defaulted. After the cross validation, the regular hyperparameter  $C$  in linear SVM was set to  $10^5$  for PB and 10 for PI. PB vectors were generated with iteration  $N = 100$ , grid size  $h = 10$  fixed, and  $\varepsilon = 0, 0.005, 0.010, 0.050, 0.100$  in eminence function. For PI, we set  $\sigma = 0.001$  and resolution to 10 to optimize the performance.

Three kernel methods, SWK, PWGK, and PSSK were evaluated on the SVM classifier, adjusting the hyperparameters of PWGK to optimize performances. In PWGK, the best performance according to cross validation was achieved when the parameters of the weighted function were set as  $K = 100, \rho = 0.01$ . In kernel SVM, the hyperparameter

Table 8: Classification accuracy of PI, PB from point clouds of seven classes containing 1970 models in total through five classifiers ( $k$ NN, RF, GBDT, LR, and LSVM), and kernel methods (SWK, PWGK, and PSSK) on SVM.

Accuracy (%)	$k$ NN	RF	GBDT	LR	LSVM
PB ( $\varepsilon = 0.000$ )	81.2%	83.0%	<b>83.4%</b>	65.5%	<b>83.4%</b>
PB ( $\varepsilon = 0.005$ )	80.6%	81.9%	82.7%	65.5%	83.0%
PB ( $\varepsilon = 0.010$ )	78.4%	80.4%	81.4%	67.8%	82.4%
PB ( $\varepsilon = 0.050$ )	76.2%	79.8%	81.1%	71.6%	81.6%
PB ( $\varepsilon = 0.100$ )	77.0%	80.0%	81.1%	74.3%	80.1%
PI	79.1%	80.5%	81.6%	82.2%	80.0%
Kernel SVM					
SWK	<b>83.8%</b>				
PWGK	80.9%				
PSSK	78.2%				

$C$  for all kernels was selected to be 10. The results are summarized in Table 8.

The SWK method shows the best performance, with the PB method with  $\varepsilon = 0$  on GBDT classifier also providing good results. Moreover, the data show that PB performance increases as the values of  $\varepsilon$  decrease. This result infers that less emphasis on the density information of points on PDs is likely to be appropriate, because more points on a PD in the  $\varepsilon$ -neighborhood of a point contribute to the eminence value as  $\varepsilon$  increases. As for the computational cost, non-learnable methods require lesser time than the kernel methods. In this experiment, the total time consumed by PB and PI was approximately 10 min, including the time spent producing vectors and training the classifiers. In comparison, kernel methods spent more than 2 h to learn from PDs (precisely, SWK 2 h; PWGK 2 h; PSSK 8 h).

Therefore, there is a trade-off between the accuracy and the computation time.

Finally, Table 9 Lists the classification accuracies of each category of the CAD models to evaluate performance of PB, PI, SWK, PWGK, and PSSK on SVM. PB has a balanced performance in each category with a good accuracy overall. SWK performs best in classifying the first three categories. In the categories of radio and wardrobe, PB performs well, while PSSK confuses between categories.

Table 9: Classification accuracy of each category of CAD models to compare performances of PB, PI, PWGK, and SWK on the classifier linear SVM.

Method/Category	Airplane	Guitar	Person	Piano	Radio	Sofa	Wardrobe
PB ( $\varepsilon = 0.0$ )	90.5%	81.5%	54.5%	77.9%	61.5%	86.4%	46.2%
PI ( $\sigma = 10^{-3}$ )	87.1%	90.5%	66.7%	69.6%	42.9%	88.4%	26.8%
SWK	93.9%	89.6%	66.7%	74.0%	40.0%	85.1%	43.8%
PWGK	88.8%	82.0%	55.6%	61.7%	64.3%	85.3%	60.0%
PSSK	87.4%	72.3%	52.9%	68.9%	0.0%	76.1%	0.0%

## 6 Discussion

In this paper, we propose a stable and efficient persistence B-spline surface generated by LSPIA as a vector representation of PDs. The PB combines the classic B-spline basis in data fitting with current tools of persistent homology in topological data analysis, and it offers a stable vector representation for numerous ML tools. We also provided a stability framework based on LSPIA with a finite number of iterations. Finally, experiments were designed to evaluate PB and its performance in classification tasks.

As the evaluation experiments show, PB vectors generated by LSPIA are efficient, insensitive to LSPIA iterations, and mildly influenced by the density of the control grid. Overall, PB can capture points with long persistence on a PD, while sometimes local density of a PD should be considered when designing the eminence function to overcome the drawback that the PB surface does not distinguish PDs that have different numbers of points in a small region. It was also experimentally shown that PB does not automatically emphasize the difference among a collection of PDs for a better performance in the test of classifying randomly generated PDs.

In the classification tasks, PB performed well under five classifiers and was computed efficiently. In comparison, the kernel method PWGK performed only slightly better in two classification tasks, requiring considerably longer computation time than PB.

From the perspective of data fitting, there are several tools to form a persistence surface based on the framework we proposed. It is worth studying the vectorizing representations via other data fitting methods and their stability with respect to traditional PD measures. Furthermore, it was found that PB vectors are sparse and that PB vectors enable the reconstruction of the persistence surfaces promptly, because PB vectors preserve the information of the control points of the persistence surfaces. (See Appendix F) Related applications of these properties must be studied further.

## Reference

- [1] Herbert Edelsbrunner, David Letscher, and Afra Zomorodian. Topological persistence and simplification. *Discrete Comput Geom*, 28:511–533, 2002.
- [2] Afra Zomorodian and Gunnar Carlsson. Computing persistent homology. *Discrete & Computational Geometry*, 33(2):249–274, 2005.
- [3] Robert Ghrist. Barcodes: the persistent topology of data. *Bulletin of the American Mathematical Society*, 45(1):61–75, 2008.
- [4] Kelin Xia and Guo-Wei Wei. Multidimensional persistence in biomolecular data. *Journal of computational chemistry*, 36(20):1502–1520, 2015.
- [5] Kelin Xia, Zhiming Li, and Lin Mu. Multiscale persistent functions for biomolecular structure characterization. *Bulletin of mathematical biology*, 80(1):1–31, 2018.
- [6] Vin De Silva and Robert Ghrist. Coverage in sensor networks via persistent homology. *Algebraic & Geometric Topology*, 7(1):339–358, 2007.
- [7] Bastian Rieck, Ulderico Fugacci, Jonas Lukasczyk, and Heike Leitte. Clique community persistence: A topological visual analysis approach for complex networks. *IEEE transactions on visualization and computer graphics*, 24(1):822–831, 2018.
- [8] Frédéric Chazal, Brittany Fasy, Fabrizio Lecci, Bertrand Michel, Alessandro Rinaldo, and Larry Wasserman. Subsampling methods for persistent homology. In *International Conference on Machine Learning*, pages 2143–2151, 2015.
- [9] Chao Chen and Novi Quadrianto. Clustering high dimensional categorical data via topographical features. In *International Conference on Machine Learning*, pages 2732–2740, 2016.
- [10] Valentin Khrulkov and Ivan V Oseledets. Geometry score: A method for comparing generative adversarial networks. *international conference on machine learning*, pages 2621–2629, 2018.
- [11] David Cohen-Steiner, Herbert Edelsbrunner, and John Harer. Stability of persistence diagrams. *Discrete & Computational Geometry*, 37(1):103–120, 2007.
- [12] Michael Kerber, Dmitriy Morozov, and Arnur Nigmatov. Geometry helps to compare persistence diagrams. *Journal of Experimental Algorithmics (JEA)*, 22:1–4, 2017.

- [13] Deepti Pachauri, Chris Hinrichs, Moo K Chung, Sterling C Johnson, and Vikas Singh. Topology-based kernels with application to inference problems in Alzheimer’s disease. *IEEE transactions on medical imaging*, 30(10):1760–1770, 2011.
- [14] Mathieu Carriere, Steve Y Oudot, and Maks Ovsjanikov. Stable topological signatures for points on 3D shapes. In *Computer Graphics Forum*, volume 34, pages 1–12. Wiley Online Library, 2015.
- [15] Barbara Di Fabio and Massimo Ferri. Comparing persistence diagrams through complex vectors. In *International Conference on Image Analysis and Processing*, pages 294–305. Springer, 2015.
- [16] Aaron Adcock, Erik Carlsson, and Gunnar Carlsson. The ring of algebraic functions on persistence bar codes. *Homology, Homotopy and Applications*, 18(1):381–402, 2016.
- [17] Sara Kališnik. Tropical coordinates on the space of persistence barcodes. *Foundations of Computational Mathematics*, pages 1–29, 2018.
- [18] Yuriy Mileyko, Sayan Mukherjee, and John Harer. Probability measures on the space of persistence diagrams. *Inverse Problems*, 27(12):124007, 2011.
- [19] Peter Bubenik. Statistical topological data analysis using persistence landscapes. *Journal of Machine Learning Research*, 16(1):77–102, 2015.
- [20] David Cohen-Steiner, Herbert Edelsbrunner, John Harer, and Yuriy Mileyko. Lipschitz functions have L p-stable persistence. *Foundations of computational mathematics*, 10(2):127–139, 2010.
- [21] Jan Reininghaus, Stefan Huber, Ulrich Bauer, and Roland Kwitt. A stable multi-scale kernel for topological machine learning. In *Proceedings of the IEEE conference on computer vision and pattern recognition*, pages 4741–4748, 2015.
- [22] David Rouse, Adam Watkins, David Porter, John Harer, Paul Bendich, Nate Strawn, Elizabeth Munch, Jonathan DeSena, Jesse Clarke, Jeff Gilbert, et al. Feature-aided multiple hypothesis tracking using topological and statistical behavior classifiers. In *Signal processing, sensor/information fusion, and target recognition XXIV*, volume 9474, page 94740L. International Society for Optics and Photonics, 2015.
- [23] Henry Adams, Tegan Emerson, Michael Kirby, Rachel Neville, Chris Peterson, Patrick Shipman, Sofya Chepushtanova, Eric Hanson, Francis Motta, and Lori

- Ziegelmeier. Persistence images: A stable vector representation of persistent homology. *Journal of Machine Learning Research*, 18(1):218–252, 2017.
- [24] Genki Kusano, Kenji Fukumizu, and Yasuaki Hiraoka. Kernel method for persistence diagrams via kernel embedding and weight factor. *Journal of Machine Learning Research*, 18(189):1–41, 2018.
- [25] Mathieu Carriere, Marco Cuturi, and Steve Oudot. Sliced wasserstein kernel for persistence diagrams. In *Proceedings of the 34th International Conference on Machine Learning-Volume 70*, pages 664–673. JMLR. org, 2017.
- [26] Tam Le and Makoto Yamada. Persistence fisher kernel: A riemannian manifold kernel for persistence diagrams. In *Advances in Neural Information Processing Systems*, pages 10027–10038, 2018.
- [27] Tullia Padellini and Pierpaolo Brutti. Supervised learning with indefinite topological kernels. *arXiv preprint arXiv:1709.07100*, 2017.
- [28] Mathieu Carrière and Ulrich Bauer. On the metric distortion of embedding persistence diagrams into separable hilbert spaces. In *35th International Symposium on Computational Geometry (SoCG 2019)*. Schloss Dagstuhl-Leibniz-Zentrum fuer Informatik, 2019.
- [29] Chongyang Deng and Hongwei Lin. Progressive and iterative approximation for least squares B-spline curve and surface fitting. *Computer-Aided Design*, 47:32–44, 2014.
- [30] Herbert Edelsbrunner and John Harer. *Computational topology: an introduction*. American Mathematical Soc., 2010.
- [31] Allen Hatcher. *Algebraic topology*. Cambridge University Press, 2002.
- [32] Herbert Edelsbrunner, Alexandr Olegovich Ivanov, and Roman Nikolaevich Karasev. Current open problems in discrete and computational geometry. Моделирование и анализ информационных систем, 19(5):5–17, 2012.
- [33] Hongwei Lin, Qi Cao, and Xiaoting Zhang. The convergence of least-squares progressive iterative approximation for singular least-squares fitting system. *Journal of Systems Science and Complexity*, 31(6):1618–1632, 2018.

- [34] Walter Rudin et al. *Principles of mathematical analysis*, volume 3. McGraw-hill New York, 1976.
- [35] Roger A Horn and Charles R Johnson. *Matrix analysis*. Cambridge University Press, 2013.
- [36] Leo Breiman. Random forests. *Machine learning*, 45(1):5–32, 2001.
- [37] Jerome H Friedman. Greedy function approximation: a gradient boosting machine. *Annals of statistics*, pages 1189–1232, 2001.
- [38] Rong-En Fan, Kai-Wei Chang, Cho-Jui Hsieh, Xiang-Rui Wang, and Chih-Jen Lin. Liblinear: A library for large linear classification. *Journal of machine learning research*, 9(Aug):1871–1874, 2008.
- [39] Ulrich Bauer. Ripser: a lean C++ code for the computation of Vietoris-Rips persistence barcodes. *Software available at <https://github.com/Ripser/ripser>*, 2017.
- [40] Jan-Martin Hertzsch, Rob Sturman, and Stephen Wiggins. DNA microarrays: design principles for maximizing ergodic, chaotic mixing. *Small*, 3(2):202–218, 2007.
- [41] Torsten Lindstrom. On the dynamics of discrete food-chains: Low- and high-frequency behavior and optimality of chaos. *Journal of Mathematical Biology*, 45(5):396–418, 2002.
- [42] George Osipenko. *Dynamical systems, graphs, and algorithms*. Springer, 2006.
- [43] Zhirong Wu, Shuran Song, Aditya Khosla, Fisher Yu, Linguang Zhang, Xiaoou Tang, and Jianxiong Xiao. 3D shapenets: A deep representation for volumetric shapes. In *Proceedings of the IEEE conference on computer vision and pattern recognition*, pages 1912–1920, 2015.
- [44] Les Piegl and Wayne Tiller. *The NURBS book*. Springer Science & Business Media, 2012.
- [45] NP Karampetakis. Computation of the generalized inverse of a polynomial matrix and applications. *Linear Algebra and its Applications*, 252(1-3):35–60, 1997.
- [46] Vladimir Rakočević. On continuity of the Moore-Penrose and Drazin inverses. *Matematički Vesnik*, 49(3-4):163–172, 1997.

## A Appendix: Preliminary of Homology

In this section, homology set up on simplicial complex is introduced. Although there are several theories of homology developed on different topological objects, such as singular complex, simplicial complex offers one an intuitive understanding of homology.

### A.1 Simplicial Homology

Given a point set  $P$  with finite number of points in  $\mathbb{R}^d$ ,  $x = \sum_{i=0}^n \lambda_i p_i$  denotes a convex combination (of course an affine combination) satisfying  $\sum_{i=0}^n \lambda_i = 1$  for each non-negative  $\lambda_i \in \mathbb{R}$ . The convex hull is the set of all the convex combinations. For  $1 \leq i \leq n$  and  $p_i \in Q \subset P$ , if the  $n$  vectors  $p_i - p_0$ , then it is called that the given  $n + 1$  points are affinely independent.

**Definition A.1** (simplex). *An  $n$ -simplex is the convex hull of  $n + 1$  affinely independent points  $Q = \{p_0, \dots, p_n\}$ , denoted as  $[p_0, p_1, \dots, p_n]$ .*

$n$  is defined to be the dimension of a simplex. For special cases, one calls vertex 0-simplex, edge 1-simplex, triangle 2-simplex, and tetrahedron 3-simplex. A face of an  $n$ -simplex  $\sigma$  is the convex hull of a proper and non-empty subset of  $Q$ , which is also a simplex denoted as  $\tau$ .

**Definition A.2** (simplicial complex). *A simplicial complex  $K$  is a finite set of simplices satisfying*

- (a) if  $\sigma \in K$  and  $\tau$  is a face of  $\sigma$ , then  $\tau \in K$ ,
- (b) and if  $\sigma_1, \sigma_2 \in K$ , then  $\sigma_1 \cap \sigma_2$  is either empty or a face of  $\sigma_1$  and  $\sigma_2$ .

The topological holes can be described in the context of combinations of  $n$ -simplices and the relationship between two combination collections with their dimensions close to each other. More precisely, for a simplicial complex  $K$ , we define a series of vector spaces  $C_n$  over a field  $\mathbb{F}$  (such as the finite field  $\mathbb{Z}_2$ ). For each  $n$ , vector space  $C_n$  is linearly spanned by a basis of all  $n$ -simplices. An  $n$ -chain in  $C_n$  is written as  $c = \sum \alpha_i \sigma_i$  where  $\sigma_i$  represents an  $n$ -simplex. And the *boundary operator*  $\partial_n : C_n \rightarrow C_{n-1}$  is a linear map defined by

$$\partial_n([p_0, p_1, \dots, p_n]) = \sum_{i=0}^n (-1)^i [p_0, \dots, \hat{p}_i, \dots, p_n],$$

where  $[p_0, \dots, \hat{p}_i, \dots, p_n]$  is the convex combination by deleting the point  $p_i$ . Chain spaces are connected with boundary operators to form a *chain complex*,

$$\dots \xrightarrow{\partial_{n+2}} C_{n+1} \xrightarrow{\partial_{n+1}} C_n \xrightarrow{\partial_n} C_{n-1} \xrightarrow{\partial_{n-1}} \dots,$$

For each  $n$ ,  $\partial_n \circ \partial_{n+1}c = 0, \forall c \in C_{n+1}$ . The boundary operators  $\partial_n$  and  $\partial_{n+1}$  induce two subspaces of  $C_n$ , the  $n$ -cycle  $Z_n = \text{Ker}\partial_n$ , and the  $n$ -boundary  $B_n = \text{Im}\partial_{n+1}$ . An element  $c$  in the  $n$ -cycle space  $Z_n$  represents a cycle because it has no boundary, i.e.,  $\partial_n(c) = 0$ , and an element in the  $n$ -boundary space  $B_n$  represents a boundary because it is the boundary of a certain  $n + 1$ -chain. Since  $\partial_n \circ \partial_{n+1}(c) = 0$ ,  $n$ -boundary space is a subspace of  $n$ -cycle space. Thus, one can take quotients to define the spaces of homology.

**Definition A.3** (simplicial homology). *The  $n$ -th homology space over a finite field  $\mathbb{F}$  is the  $n$ -th cycle space modulo the  $n$ -th boundary space, i.e.,  $H_n = Z_n/B_n$ . And the Betti number is the dimension of  $H_n$ , denoted as  $\beta_n$ .*

An element in  $n$ -homology space is an equivalent class, called homological class, which represents holes in topological space. Please refer to the textbook Hatcher (2002) [31] for a further reading and Edelsbrunner and Harer (2010) [30] section IV for a short introduction.

## A.2 Simplicial Complex for Point Clouds

Simplicial complex offers one an approach to compute the Betti numbers of a topological space. In order to evaluate the topology of a point cloud, a simplicial complex needs constructing on it. Vietoris-Rips complex and the Čech complex are two commonly used tools to generate a complex sequence on a point cloud. Given a finite collection of data points  $P = \{p_i\}$  in a metric space  $(\mathbb{X}, d)$  and a parameter  $\epsilon \geq 0$ , a *Vietoris-Rips complex* is defined by

$$VR(\epsilon) = \{\sigma = [p_0, \dots, p_n] \mid B(p_i, \epsilon) \cap B(p_j, \epsilon) \neq \emptyset, \quad \forall p_i, p_j \in \{p_0, \dots, p_n\}\},$$

and a *Čech complex* is defined by

$$C(\epsilon) = \{\sigma = [p_0, \dots, p_n] \mid \bigcap_{i=0, \dots, n} B(p_i, \epsilon) \neq \emptyset, \quad \forall i = 0, \dots, n, p_i \in P\},$$

where  $B(p, \epsilon)$  is a closed ball with its center  $p$  and its radius  $\epsilon$ . For the same  $\epsilon$ , we have  $C(\epsilon) \subseteq VR(\epsilon) \subseteq C(\sqrt{2}\epsilon)$ , in which the first part comes immediately from the definitions. Meanwhile, the V-R complex can be realized to be an approximation of the Čech complex. And notice another fact that if  $\epsilon_i \leq \epsilon_j$ , then  $VR(\epsilon_i) \subseteq VR(\epsilon_j)$  and  $C(\epsilon_i) \subseteq C(\epsilon_j)$ . As  $\epsilon$  increases, it induces a filtered sequence, over which one can compute persistent homology groups to detect persistent homological features.

### A.3 Filtrations from Functions

Given a topological space  $\mathbb{X}$ ,  $f : \mathbb{X} \rightarrow \mathbb{R}$  is a scalar function. Define a *sublevel set* by  $f^{-1}(-\infty, a] = \{x \in \mathbb{X} | f(x) \leq a\}$  which consists of all points with its scalar value at most  $a$ . It induces a filtration of the topological space  $\mathbb{X}$  from the function  $f$ , if there is a series of scalar values  $a_0 \leq a_1 \leq \dots \leq a_m$ , then

$$f^{-1}(-\infty, a_0] \subseteq f^{-1}(-\infty, a_1] \subseteq \dots \subseteq f^{-1}(-\infty, a_m].$$

From the perspective of function, one can define a distance function on a data set  $P$  in a metric space  $(\mathbb{X}, d)$ . Let  $f_d(x) = \inf_{p_i \in P} d(p_i, x)$  for all points  $x \in \mathbb{X}$ . Then the filtration by  $f_d(x)$  induces the Čech complex on  $P$ .

## B Appendix: B-Spline and LSPIA

The idea of data fitting is commonly used in regression analysis on the questions of statistical inference to deduce the possible probability distributions, and to visualize the data so that the potential tendency can be extracted. One of efficient methods to fit a large set of data is progressive and iterative approximation for least squares B-spline surface fitting (LSPIA) [29], which generates smooth approximation B-spline surfaces on a 3D data set. A brief introduction on B-spline surface and LSPIA is offered to readers. For more knowledge about B-spline, please see the textbooks such as Piegl (1997) [44].

### B.1 B-Spline Surface

A *B-spline*, also called basis spline, of order  $n$  is a piecewise polynomial function of degree  $n - 1$  with a variable  $t$ . A series of non-decreasing sequence  $\{\dots \xi_{i-1}, \xi_i, \xi_{i+1}, \dots\}$  denotes *knots* at which the pieces of polynomials join. Given a sequence of knots, the B-splines of order 1 are defined by

$$B_{i,1}(t) = \begin{cases} 1 & \xi_i \leq t < \xi_{i+1} \\ 0 & \text{otherwise} \end{cases}$$

The B-splines of  $(k + 1)$ st-order are defined in the way of recursion by

$$B_{i,k+1}(t) = \frac{t - \xi_i}{\xi_{i+k} - \xi_i} B_{i,k}(t) + \frac{\xi_{i+k+1} - t}{\xi_{i+k+1} - \xi_{i+k}} B_{i+1,k}(t)$$

A collection of B-splines has the weight property, i.e.  $\sum_{i=0}^n B_i(t) = 1$ .

A  $(p - 1)$ st-degree uniform *B-spline surface*, of which the order is  $p$ , is defined by

$$S(s, t) = \sum_{i=0}^n \sum_{j=0}^n \mathbf{P}_{ij} B_{i,p}(s) B_{j,p}(t) \quad s, t \in [0, 1]$$

where  $\{\mathbf{P}_{ij}\}$  are the *control points* in 3D, and the  $p$ th-degree B-spline basis functions  $B_{i,p}(s)$  and  $B_{j,p}(t)$  are defined respectively on the uniform knot sequences on  $[0, 1]$

$$S = \{\underbrace{0, \dots, 0}_p, s_1, \dots, s_{n-1}, \underbrace{1, \dots, 1}_p\} \quad T = \{\underbrace{0, \dots, 0}_p, t_1, \dots, t_{n-1}, \underbrace{1, \dots, 1}_p\}$$

which makes the property of endpoint interpolation hold.

In PB, we use a uniform cubic uniform B-spline surface, where  $p = 4$ , for data fitting.

## B.2 LSPIA: Convergence and Computational Complexity

Intuitively, LSPIA for B-spline surfaces begins with an initial blending surface (eg. the plane  $z = 0$ , and the  $z$ -coordinates of initial control points are zero), and adjusts the control points by a weighting sum of difference vectors between measured points and their corresponding points on the fitting surface generated by previous control points to construct the fitting surface iteratively.

Given a 3D data set  $\{\mathbf{Q}_l\}_{l=1}^k$  where each  $\mathbf{Q}_l = (s_l, t_l, q_l)$ , assume that each  $(s_l, t_l)$  is in the range of  $[0, 1]^2$ . Before the iteration, the control points  $\{\mathbf{P}_{ij}\}_{i,j=0}^n$ , where each  $\mathbf{P}_{ij} = (s_i, t_j, p_{ij})$ ,  $(s_i, t_j) \in [0, 1]^2$ , is initialized. For each  $\mathbf{P}_{ij}^{(0)} = (s_i, t_j, p_{ij}^{(0)})$ , let  $\{(s_i, t_j)\}$  be the vertices of a uniform grid on  $[0, 1]^2$  and  $p_{ij}^{(0)} = 0$ . The initial surface is constructed by

$$S^{(0)}(s, t) = \sum_{i=0}^n \sum_{j=0}^n p_{ij}^{(0)} B_i(s) B_j(t) \quad s, t \in [0, 1]$$

Let  $\delta_l^{(0)} = q_l - S^{(0)}(s_l, t_l)$  be the difference vector between measured data and the corresponding points on the surface  $S^{(0)}$ . And take the initial adjusting matrix of the control points as

$$\Delta_{ij}^{(0)} = \mu \sum_{l=1}^k B_i(s_l) B_j(t_l) \delta_l^{(0)}.$$

where  $0 < \mu < 2/\lambda_0$  is a constant and  $\lambda_0$  is the largest eigenvalue of  $\mathbf{B}^T \mathbf{B}$ . Then add the adjusting matrix to the matrix of the control points  $[p_{ij}^{(0)}]$ . We obtain the new control points  $\mathbf{P}_{ij}^{(1)} = (s_i, t_j, p_{ij}^{(1)})$ , where

$$p_{ij}^{(1)} = p_{ij}^{(0)} + \Delta_{ij}^{(0)},$$

which generates a new surface  $S^{(1)}$ . Hence, in the  $h$ th iteration, the  $h$ th surface is gotten.

Then we have

$$\begin{aligned}\delta_l^{(h)} &= q_l - S^{(h)}(s_l, t_l) \\ \Delta_{ij}^{(h)} &= \mu \sum_{l=1}^k B_i(s_l) B_j(t_l) \delta_l^{(h)} \\ p_{ij}^{(h+1)} &= p_{ij}^{(h)} + \Delta_{ij}^{(h)}\end{aligned}$$

and  $(h + 1)$ st surface

$$S^{(h+1)}(s, t) = \sum_{i=0}^n \sum_{j=0}^n p_{ij}^{(h)} B_i(s) B_j(t) \quad s, t \in [0, 1].$$

The iteration will pause once the number of iteration is satisfied.

In the PB, let  $c_{i,j} = \sum_{l=1}^k B_i(s_l) B_j(t_l)$ , for  $i, j = 1, \dots, h$ , respectively, and  $C := \max_{1 \leq i, j \leq h} \{c_{i,j}\}$ . Note that  $C \neq 0$ . Then, one can take  $\mu_{ij} = 1/C$  that is, for different  $i$  and  $j$ , the weights  $\mu_{ij}$  are the same.

The following theorem gives the convergence of LSPIA in Lin et al. (2017) [33].

**Theorem B.1.** *Suppose that  $\mathbf{B}$  is the B-spline basis matrix given by equation (10). If  $\mathbf{B}^T \mathbf{B}$  is singular, and the spectral radius  $\rho(\Lambda \mathbf{B}^T \mathbf{B}) \leq 1$ , the iterative method 12 converges to the M-P pseudo-inverse solution of the linear system  $\mathbf{B}^T \mathbf{B} \tilde{\mathbf{Z}} = \mathbf{B}^T \mathbf{Z}$  (refer to equation (5)). Moreover, if the initial value  $\tilde{\mathbf{Z}}^{(0)} = \mathbf{O}$ , the iterative method converges to  $\mathbf{B}^+ \mathbf{Z}$ , i.e., the M-P pseudo-inverse solution of the linear system with the minimum Euclidean norm, where  $\cdot^+$  represents the M-P pseudo-inverse of a matrix.*

According to the theorem above, the convergence of LSPIA in our PB method is given by the following corollary.

**Corollary 1.** *The LSPIA method (equation 12) for persistence B-spline surface is convergent.*

*Proof.* The iterative format is rewritten in matrix form with the initial condition  $\tilde{\mathbf{Z}}^{(0)}$ :

$$\tilde{\mathbf{Z}}^{(p+1)} = (\mathbf{E} - \Lambda \mathbf{B}^T \mathbf{B}) \tilde{\mathbf{Z}}^{(p)} + \Lambda \mathbf{B}^T \mathbf{Z},$$

where  $\Lambda = \text{diag}(1/C, 1/C \dots, 1/C)$  is a diagonal matrix, and

$$C = \max_{1 \leq i, j \leq h} \left\{ \sum_{l=1}^k B_i(s_l) B_j(t_l) \right\} \neq 0.$$

It is supposed to prove that the eigenvalues  $\lambda$  of the matrix  $\mathbf{\Lambda B}^T \mathbf{B}$  satisfy  $0 \leq \lambda \leq 1$ , which matches the condition of Theorem B.1. Since the B-spline basis has the weight property,  $\|\mathbf{B}\|_\infty = 1$ , where  $\|\cdot\|_\infty$  denotes the induced  $\infty$ -norm of a matrix. And since

$$\sum_{i=1}^k \frac{B_*(s_i)B_*(t_i)}{C} \leq \sum_{i=1}^k \frac{B_*(s_i)B_*(t_i)}{\sum_{l=1}^k B_*(s_l)B_*(t_l)} = 1,$$

we have  $\|\mathbf{\Lambda B}^T\|_\infty \leq 1$  and

$$\|\mathbf{\Lambda B}^T \mathbf{B}\|_\infty \leq \|\mathbf{\Lambda B}^T\|_\infty \|\mathbf{B}\|_\infty \leq 1$$

Hence, it follows from Theorem 5.6.9 in Horn et al (2013) [35] that the eigenvalue  $\lambda$  of the matrix  $\mathbf{\Lambda B}^T \mathbf{B}$  satisfies  $\lambda \leq \|\mathbf{\Lambda B}^T \mathbf{B}\|_\infty \leq 1$ . According to Theorem B.1, the LSPIA for PB is convergent.  $\square$

Finally, the computational complexity and memory cost per iteration step of the LSPIA method are measured. Note that the matrix  $\mathbf{B}$  is of  $k \times h^2$ , and  $\mathbf{Z}$  is of  $k \times 1$ . Then, each iteration step of the LSPIA method needs  $(2k + 1)h^2$  multiplications and  $2kh^2$  additions. And in each iteration, it is required to store two  $h^2 \times 1$  vectors,  $\tilde{\mathbf{Z}}^{(\beta)}$  and  $\tilde{\mathbf{Z}}^{(\beta+1)}$ , one  $k \times 1$  vector  $\mathbf{Z}$ , and one  $k \times h^2$  matrix  $\mathbf{B}$ . Therefore, each iteration requires  $(k + 2)h^2 + k$  unit memory. It is supposed to be mentioned that, in the large scale data fitting, the matrix  $\mathbf{B}$  is usually sparse, and the computational complexity and memory requirement will be greatly reduced.

## C Stability Theorem in the Condition of $N \rightarrow \infty$

According to Theorem B.1 and Corollary 1, it is proved that the result of LSPIA converges to the M-P pseudo-inverse solution of the linear system with the minimum Euclidean norm. In other words, the matrix  $\mathbf{B}$  defined in equation (14) converges to the M-P pseudo-inverse matrix  $\mathbf{B}^+$  of the basis matrix  $\mathbf{B}$  in the linear system (5). In Section 4, the continuity of the matrix of functions  $\bar{\mathbf{B}}$  is analyzed in Lemma 4.5 with a finite number of iteration of LSPIA  $N$ . Here, a similar result about the continuity of the matrix  $\mathbf{B}^+$  is given under an assumption of a slight perturbation of PD. And then, the stability theorem holds by replacing  $\bar{\mathbf{B}}$  with  $\mathbf{B}^+$ .

First, the least-squares solution of a system of linear equations is obtained by the following theorem which is usually introduced in the textbooks of linear algebra.

**Theorem C.1.** *For a system of linear equations  $\mathbf{Bx} = \mathbf{b}$ , where  $\mathbf{B} \in \mathbb{R}^{m \times n}$ , the least-squares solution of the system is given by*

$$\mathbf{x} = \mathbf{B}^+ \mathbf{b} + (\mathbf{I} - \mathbf{B}^+ \mathbf{B})\mathbf{y},$$

where  $\mathbf{B}^+$  is the Moore-Penrose (M-P) pseudo-inverse matrix of matrix  $\mathbf{B}$ .  $\mathbf{y}$  is an arbitrary vector in  $\mathbb{R}^n$ . And  $\tilde{\mathbf{x}} = \mathbf{B}^+\mathbf{b}$  is the unique least-squares solution which makes  $\|\tilde{\mathbf{x}}\|_2 \leq \|\mathbf{x}\|_2$  hold.

As a result, one can express the least-squares solution with the minimum Euclidean norm of the system  $\mathbf{B}\tilde{\mathbf{Z}} = \mathbf{Z}$  to be  $\tilde{\mathbf{Z}} = \mathbf{B}^+\mathbf{Z}$ . And then, it is necessary to check the stability of  $\tilde{\mathbf{Z}}$ , that is, to prove that the matrix  $\mathbf{B}^+$  is stable with respect of a small perturbation. Observe that the matrix  $\mathbf{B}$  can be referred to as a matrix of functions of which the variables are  $(s_1, t_1, \dots, s_k, t_k) \in \mathbb{R}^{2k}$ . In this view, one can expand the matrix  $\mathbf{B}$  to be a polynomial matrix, i.e.,

$$\mathbf{B}(s_1, t_1, \dots, s_k, t_k) = \mathbf{B}_{q_1 q_2 \dots q_{2k}} s_1^{q_1} t_1^{q_2} \dots s_k^{q_{2k}} + \dots + \mathbf{B}_{0,0,\dots,1} s_n + \mathbf{B}_{0,0,0,\dots,0} \quad \mathbf{B}_* \in \mathbb{R}^{k \times h^2}$$

which is a multi-variable polynomial, in a lexicographical order, with its coefficients being matrices.

For a further analysis, the explicit expression of  $\mathbf{B}^+$  is given by the following theorem, which is provided in Section 3.1 of [45].

**Theorem C.2.** Let  $\mathbf{s} \in \mathbb{R}^{2k}$  be the variable  $(s_1, t_1, \dots, s_k, t_k)$ ,  $\mathbf{B}(\mathbf{s}) \in \mathbb{R}^{m \times n}$  be a polynomial matrix, and

$$\begin{aligned} a(\lambda, \mathbf{s}) &= \det[\lambda \mathbf{E}_m - \mathbf{B}(\mathbf{s})\mathbf{B}(\mathbf{s})^T] \\ &= \lambda^m + a_1(\mathbf{s})\lambda^{m-1} + \dots + a_{m-1}(\mathbf{s})\lambda + a_m(\mathbf{s}) \end{aligned}$$

be the characteristic polynomial of  $\mathbf{B}(\mathbf{s})\mathbf{B}(\mathbf{s})^T$ , where  $a_*(\mathbf{s})$  represents a function. Let  $a_m(\mathbf{s}) = 0, \dots, a_{r+1}(\mathbf{s}) = 0$  while  $a_r(\mathbf{s}) \neq 0$  and  $\Lambda := \{(\mathbf{s}) \in \mathbb{R}[(\mathbf{s})] : a_r(\mathbf{s}) = 0\}$ . Then the M-P pseudo-inverse matrix  $\mathbf{B}(\mathbf{s})^+$  of  $\mathbf{B}(\mathbf{s})$  for  $\mathbf{s} \in \mathbb{R}^{2k} \setminus \Lambda$  is given by

$$\mathbf{B}(\mathbf{s})^+ = -a_r(\mathbf{s})^{-1} \mathbf{B}(\mathbf{s})^T [(\mathbf{B}(\mathbf{s})\mathbf{B}(\mathbf{s})^T)^{r-1} + a_1(\mathbf{s})(\mathbf{B}(\mathbf{s})\mathbf{B}(\mathbf{s})^T)^{r-2} + \dots + a_{r-1} \mathbf{E}_m]$$

If  $r = 0$ , then  $\mathbf{B}(\mathbf{s})^+ = \mathbf{O}$ . For those  $\mathbf{s}_i \in \Lambda$ , find the largest integer  $r_i < r$  such that  $a_{r_i}(\mathbf{s}) \neq 0$  and then the M-P pseudo-inverse matrix  $\mathbf{B}(\mathbf{s})^+$  of  $\mathbf{B}(\mathbf{s})$  is given by

$$\mathbf{B}(\mathbf{s}_i)^+ = -a_{r_i}(\mathbf{s}_i)^{-1} \mathbf{B}(\mathbf{s}_i)^T [(\mathbf{B}(\mathbf{s}_i)\mathbf{B}(\mathbf{s}_i)^T)^{r_i-1} + a_1(\mathbf{s}_i)(\mathbf{B}(\mathbf{s}_i)\mathbf{B}(\mathbf{s}_i)^T)^{r_i-2} + \dots + a_{r_i-1} \mathbf{E}_m].$$

Notice that the M-P pseudo-inverse matrix of a matrix of continuous functions is continuous in a certain condition. The following theorem (Theorem 4.2 in [46]) gives the necessary and sufficient condition to make the M-P pseudo-inverse matrix continuous.

**Theorem C.3.** If there is a series of  $\mathbf{B}_i \in \mathbb{R}^{m \times n}$ ,  $\mathbf{B} \in \mathbb{R}^{m \times n}$  and  $\mathbf{B}_i \rightarrow \mathbf{B}$ , then

$$\mathbf{B}_i^+ \rightarrow \mathbf{B}^+ \quad \iff \quad \exists i_0 \text{ s.t. for } i \geq i_0, \quad \text{rank} \mathbf{B}_i = \text{rank} \mathbf{B}$$

If the perturbation on a PD is properly small so that it makes the M-P pseudo-inverse matrix  $\mathbf{B}^+$  keep the same rank w.r.t. the variables in a closed interval, then  $\mathbf{B}^+$  is continuous w.r.t. the variables. Therefore, we make an assumption as follows.

**Assumption 1.** *Assumed that if  $W_p(PD^{(1)}, PD^{(2)}) \leq \tau$ , there exists a closed interval  $H \subset [0, 1]^{2k}$  determined by  $\tau$  such that for  $(s_1, t_1, \dots, s_k, t_k) \in H$ ,  $\mathbf{B}(s_1, t_1, \dots, s_k, t_k)$  has the same rank with respect to variables.*

Under this assumption,  $\mathbf{B}^+(s_1, t_1, \dots, s_k, t_k)$  is continuous in the closed interval  $H$ . And  $(s_1^{(1)}, t_1^{(1)}, \dots, s_k^{(1)}, t_k^{(1)})$  and  $(s_1^{(2)}, t_1^{(2)}, \dots, s_k^{(2)}, t_k^{(2)})$  are in  $H$ .

**Lemma C.1.** *With the assumption above, for each  $(s_1, t_1, \dots, s_k, t_k) \in H$  and the B-spline basis matrix  $\mathbf{B}$  given by the system of linear equations, every entry in the matrix  $\mathbf{B}^+$  is a  $C^1$  continuous function w.r.t. the variables on the closed interval  $H$ .*

*Proof.*  $\mathbf{B}$  has the same rank for each  $(s_1, t_1, \dots, s_k, t_k) \in H$ . By using Theorem C.3,  $\mathbf{B}^+(s_1, t_1, \dots, s_k, t_k)$  is continuous on  $H$ . Especially,  $\mathbf{B}$  is the B-spline basis matrix, of which each entry is a cubic polynomial, which is  $C^1$ -continuous. According to Theorem C.2, the coefficient  $r$  in the explicit expression of  $\mathbf{B}^+$  is equal to the rank of  $\mathbf{B}$ , which is a constant under Assumption 1. Each entry of  $\mathbf{B}^+$  is a rational function, the quotient of two polynomials, with its numerator polynomial and its denominator polynomial  $C^1$ -continuous on  $H$ . Notice that the denominator polynomial,  $a_r(s_1, t_1, \dots, s_k, t_k)$  in the explicit expression of  $\mathbf{B}^+$ , is nonzero on  $H$ , which guarantees the  $C^1$  continuity of each entry of  $\mathbf{B}^+$ .  $\square$

Under Assumption 1, one can replace Lemma 4.5 with Lemma C.1, and replace  $\bar{\mathbf{B}}$  with  $\mathbf{B}^+$  in Theorem 4.1 to make the stability result hold. In our case, the data points scattered on the domain are regarded as variables so that the iterative matrix is a matrix of functions, i.e., each entry of the matrix is a function with respect to these variables. To guarantee the continuity of each entry of the convergent matrix, a necessary and sufficient condition is needed for the the iterative matrix  $\bar{\mathbf{B}}_N$ . Frankly speaking, the condition the data points satisfy is still ambiguous and unclear to make the condition hold. Although one can put a strong assumption on data points to make the rank of iterative matrix unchange, it restricts the situation in which the method can be used. Therefore, as a compromise, to consider the iterative matrix with a finite iteration of LSPIA is an appropriate approach to make up the gap. For a finite iteration, each entry of the iterative matrix is a rational polynomial with respect to the variables. And then, the stable coefficient can be estimated by the first partial derivatives of each entry.

## D Stable Coefficient and Iteration of LSPIA

Although the stability of PB vector is given in Theorem 4.1, it is not explicit to make clear the relation between the stable coefficient  $C_{p,m,N,\mathcal{E}}$  and the variables, where  $p$  means the  $p$ -norm chosen to measure the vectors,  $m$  depends on the range of domain where points on a PD locate,  $\mathcal{E}$  contributes the bound of first derivative of eminence function  $\mathcal{E}$  to the stable coefficient. However, instead of discussing the continuity of every entry in the iterative matrix  $\tilde{\mathbf{B}}_N$  given in Eq. 13, a situation with a finite iteration of LSPIA is set to explain the stability. To clarify the dependence between the stable coefficient and the iteration, an experiment is designed to illustrate the relationship.

Given  $PD^{(1)}$  and  $PD^{(2)}$ , the stable coefficient is evaluated by

$$C_p = \frac{\|\tilde{\mathbf{Z}}_N^{(1)} - \tilde{\mathbf{Z}}_N^{(2)}\|_p}{W_p(PD^{(1)}, PD^{(2)})}, \quad (15)$$

where  $N$  indicates the iteration with which the PB vector is produced. Without loss of generality, one can let  $PD^{(2)} = \emptyset$ , i.e., an empty diagram, which can be understood as the situation that an empty PD is perturbed to become  $PD^{(1)}$ . In this case, the stable coefficient is given by

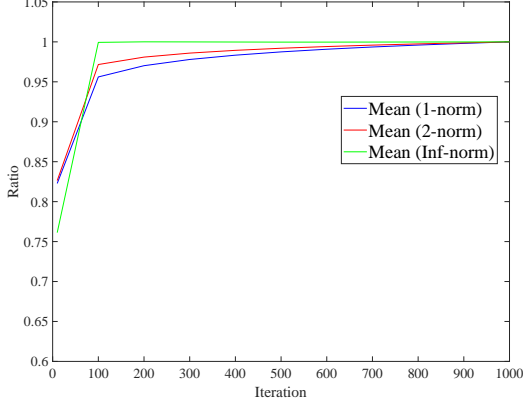
$$C_p = \frac{\|\tilde{\mathbf{Z}}_N^{(1)}\|_p}{W_p(PD^{(1)}, \emptyset)}. \quad (16)$$

To analyze the stable coefficient, one has to fix the other parameters. In the experiment, we set the domain to be  $[0, 1]^2$ , i.e.,  $m = 1$ , the size of PB grid  $20 \times 20$ , i.e., the length of PB vector 400, and  $\varepsilon = 0$  in the eminence function  $\mathcal{E}$ . Meanwhile, let the iteration  $N = 10$  as an initial value, then increase from 100 to 1000 with an increment 100. The stable coefficient  $C_p$  is computed when  $p = 1, 2$  and  $\infty$ .

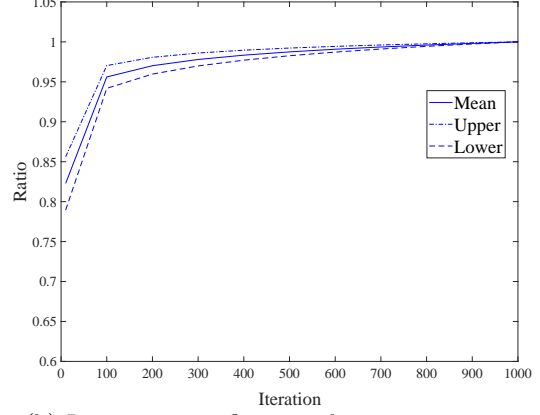
In the experiment, we generate 1000 randomly generated PDs with about 200 points on which points scatter above and close to the diagonal in the domain  $[0, 1]^2$ . The approach of producing PDs is similar to that used in the experiment of classification of randomly-generated PDs. For a PD, the corresponding PB vector with respect to different iteration  $N$  is obtained to compute the stable coefficient w.r.t. different  $N$  via eq. 16. However, for different PD, the  $W_p$  distance to empty diagram is likely to be various. So it has little meaning to compare with the stable coefficient of different PDs unless the growth rate of stable coefficient is studied. To measure the growth rate of stable coefficient w.r.t. different  $N$ , a ratio is defined by the quotient

$$R = C_{p,N_i}/C_{p,1000} = \frac{\|\tilde{\mathbf{Z}}_{N_i}^{(1)}\|_p}{W_p(PD^{(1)}, \emptyset)} / \frac{\|\tilde{\mathbf{Z}}_{1000}^{(1)}\|_p}{W_p(PD^{(1)}, \emptyset)} = \frac{\|\tilde{\mathbf{Z}}_{N_i}^{(1)}\|_p}{\|\tilde{\mathbf{Z}}_{1000}^{(1)}\|_p} \quad (17)$$

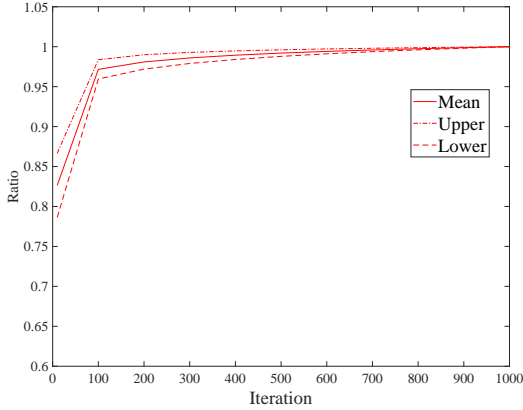
where  $C_{p,N_i}$  is the stable coefficient with iteration  $N = N_i$ , and  $i = 10, 100, \dots, 900$ . It allows us to do statistics on the ratio correspond to each randomly generated PD, and mean value and standard deviation of the ratios are given in Figure 6.



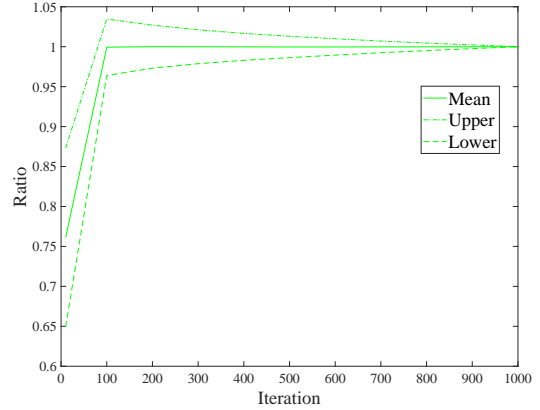
(a) Mean value of the ratios with different norms  $p = 1, 2, \infty$



(b) Iteration-ratio figure with norm  $p = 1$



(c) Iteration-ratio figure with norm  $p = 2$



(d) Iteration-ratio figure with norm  $p = \infty$

Figure 6: Iteration-ratio figures: for  $p = 1, 2$  and  $\infty$ , respectively, the mean value and the standard deviation of the ratios (eq. 17) of  $p$ -norm of PB vectors based on 1000 randomly-generated PDs are computed, and the curve of mean value, the curves of upper bound and of lower bound are estimated.

As shown in Figure 6, the ratios of stable coefficient with respect to different  $p$ -norm increase when the iteration  $N$  changes from 10 to 100, and then they increase quite slowly and remain nearly stable when  $N$  increases until  $N = 1000$ . Meanwhile, the variation of the ratios computed on the dataset of 1000 randomly-generated PDs is more and more subtle when  $N$  grows larger as shown by the dashed lines in Figure 6 that upper and lower bounds of the ratios are close to the mean value, which reaches nearly 1.

For a concrete example, in the subfigure (b), (c) and (d) of Figure 6, when the iteration increases twice from 500 to 1000, the stable coefficient with  $p = 1, 2$  and  $\infty$  increases 1.03, 1.02, 1.00 times in average, respectively. It suggests that stable coefficient w.r.t. different  $p$ -norm has inclination to maintain stable when the iteration increases. In other words, if only the iteration is adequate, in this case,  $N = 100$ , the stable coefficient will increase quite slowly as  $N$  increases. And it offers an evidence to eliminate the doubt that the iteration  $N$  has a prominent influence on stable coefficient.

## E Appendix: Details in Experiments

### E.1 Examples in the Tests of Extracted Features via PB

In the first test, we design five categories in each of which location of the points with long persistence is distinct. A random PD follows the form  $(x - \tau|y|/2, x + \tau|y|/2)$ , where  $x$  is drawn uniformly in  $[0, 1]$ ,  $y$  is chosen from another normal distribution  $N(0, 1)$ , and  $\tau$  is a positive constant. And a random PD mentioned above is denoted as  $PD_r$ . Let  $\mathbf{P}_1 = (0.1, 0.8)$ ,  $\mathbf{P}_2 = (0.3, 0.7)$ ,  $\mathbf{P}_3 = (0.7, 0.9)$ . In both tests, we set  $\tau = 0.02$  and the number of points close to the diagonal is 50.  $\bar{\mathbf{P}}_i$  denotes the point  $\mathbf{P}_i$  with a small perturbation, where  $i = 1, 2, 3$ . In details, we take  $\bar{\mathbf{P}}_i = (x_i \pm \tau \cdot r_1, y_i \pm \tau \cdot r_2)$ , where  $\mathbf{P}_i = (x_i, y_i)$ , and  $r_1$  and  $r_2$  are random numbers in the interval  $(0, 1)$ .

In the second test, PDs in five categories are produced by  $PD_r$ ,  $PD_r \cup \bar{\mathbf{P}}_1$ ,  $PD_r \cup \bar{\mathbf{P}}_2$ ,  $PD_r \cup \bar{\mathbf{P}}_3$  and  $PD_r \cup \bar{\mathbf{P}}_2 \cup \bar{\mathbf{P}}_3$ , respectively. Examples of a single PD in each of five categories are shown in Figure 7. In the second test, PDs of five categories of PDs are produced as follows: a PD in  $i$ th category is a union of a random PD and  $i$  perturbed  $\bar{\mathbf{P}}_1$ 's, where  $i = 1, 2, \dots, 5$ . Examples of PDs are given in Figure 8.

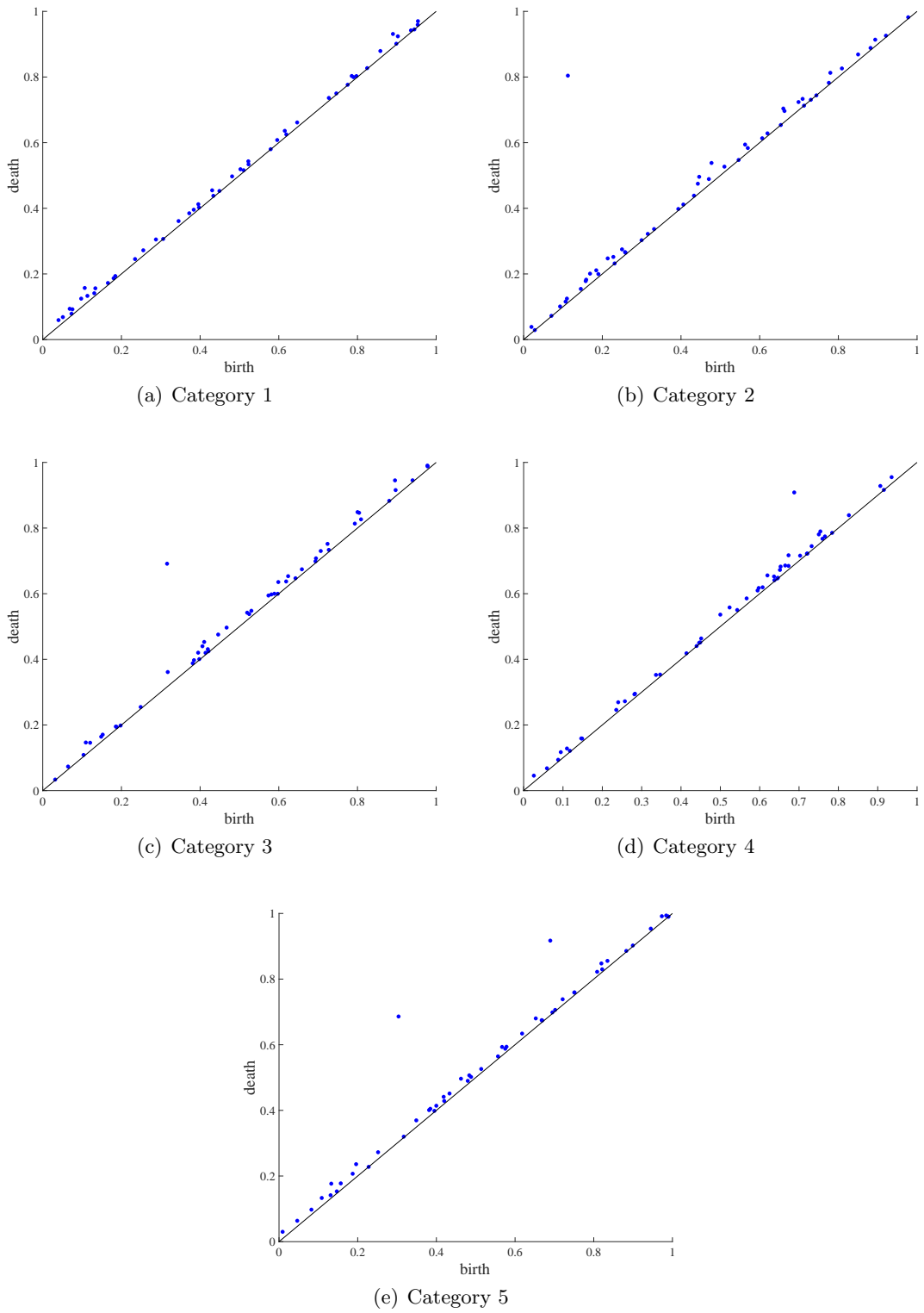
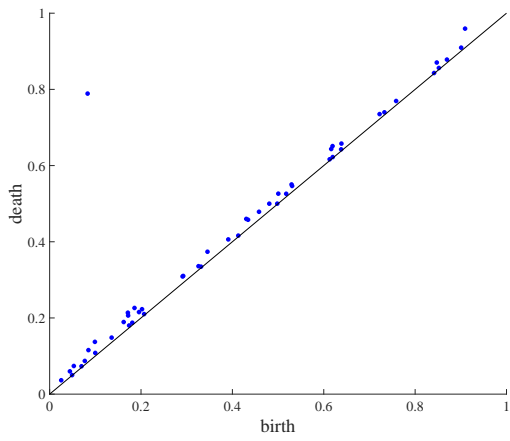
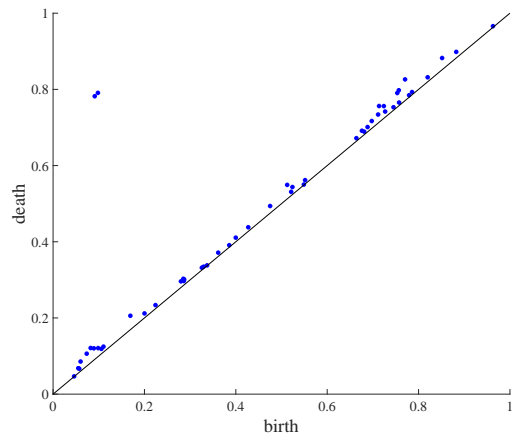


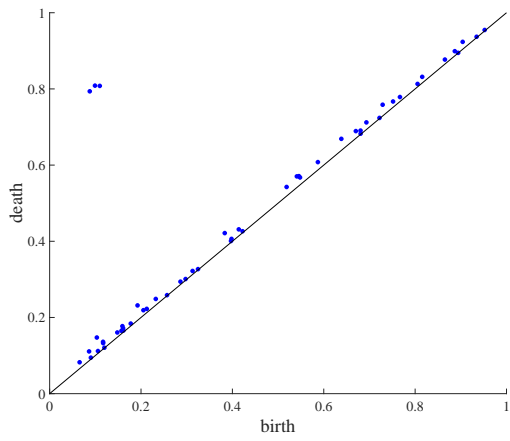
Figure 7: Examples of a PD in each of five categories in the first test of randomly generated PDs to evaluate PB method.



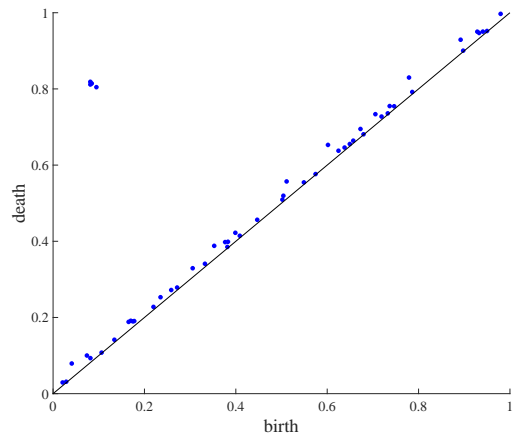
(a) Category 1



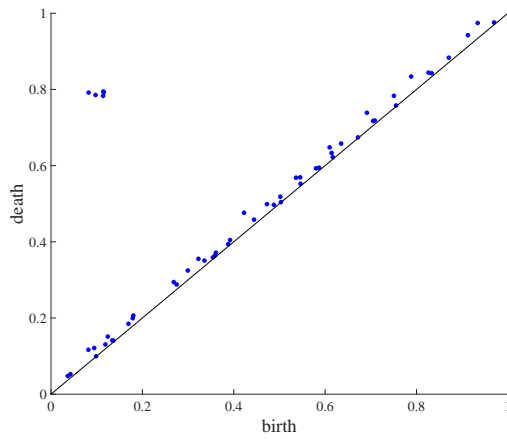
(b) Category 2



(c) Category 3



(d) Category 4



(e) Category 5

Figure 8: Examples of a PD in each of five categories in the second test of randomly generated PDs to evaluate PB method.

## E.2 Subcategory of ModelNet40

In the experiment of ModelNet40, PB is tested on a subcategory of ModelNet40 where there are 7 categories of CAD models. The categories are selected according to the principles that (1) more difference of topology between each category is emphasized, and (2) less shape semantics is involved. The benchmark contains 12,311 CAD models divided into 40 object categories. All categories with their name and index are listed as follows: airplane (0), bathtub (1), bed (2), bench (3), bookshelf (4), bottle (5), bowl (6), car (7), chair (8), cone (9), cup (10), curtain (11), desk (12), door (13), dresser (14), flower pot (15), glass box (16), guitar (17), keyboard (18), lamp (19), laptop (20), mantel (21), monitor (22), night stand (23), person (24), piano (25), plant (26), radio (27), range hood (28), sink (29), sofa (30), stairs (31), stool (32), table (33), tent (34), toilet (35), tv stand (36), vase (37), wardrobe (38), and xbox (39).

Meanwhile, the selected categories are shown in Table 10. Notice that the number of models contained in each category is not the same. There are 1970 CAD models in total in the selected subcategory.

Table 10: the categories selected in the experiment of classifying 3D CAD models to evaluate the methods.

Item/Category	Piano	Person	Airplane	Radio	Guitar	Wardrobe	Sofa
Index	25	24	0	27	17	38	30
Number of Models	231	88	625	104	155	87	680

## F Visulization and Reconstruction of Persistence Surfaces

In the experiment of determining parameters of the 3D dynamical system, the parameters  $M_1 = 1.0$ ,  $M_2 = M_3 = 4.0$  were fixed, and the parameter  $M_0$  was set to be

$$3.0, 3.3, 3.48, 3.54, 3.57, 3.532, 3.571, 3.3701, 3.4001,$$

respectively, to generate nine classes of data. For each class, the initial value  $(X_0, Y_0, Z_0)$  was taken randomly from  $(1, 2) \times (0, 1)^2$ . The dynamical system was iterated 2000 times to obtain 2000 points in the 3D Euclidean space. Meanwhile, it was repeated 50 times under the combination of the parameters of the 3D dynamical system to obtain 50 collections of points. One of the original data with certain initial value in first three class are shown in the left figure of Figure 9-11.

Then, the V-R complex was constructed on each collection of points, and the filtration was generated to compute the PD as an output. The corresponding PD of the

original data is shown in the middle figure of Figure 9-11. The persistence grids were computed by the proposed method, and the persistence vectors were used in the task of classification of original data with different parameters. Then, the accuracy of classification was figured out under each classifier to check whether the proposed method was effective.

Furthermore, it is noticed that given the control points of a cubic uniform B-spline surface, the surface can be precisely reconstructed. It is shown in the right figure of Figure 9-11 that the PB vectors preserve the complete information of the persistence surfaces. Meanwhile, the proposed method provides a tool of visualization, by which the geometric information of a persistence vector is illustrated.

Eventually, it is founded that about 90% of entries of a persistence vector are zero, that is, the PB vectors are sparse. It is potential to explore the classification approach for the sparse PB vectors.

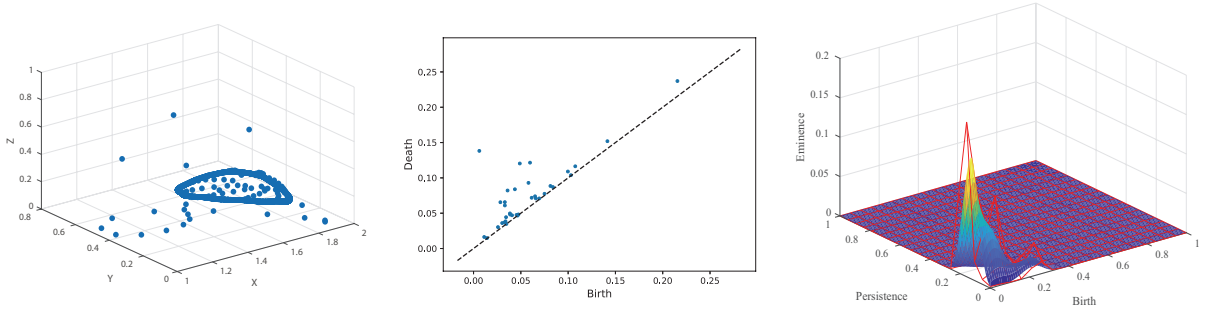


Figure 9: An example in the class of  $M_0 = 3.0$ . Left figure: the data points are generated by the 3D dynamical system with  $M_0 = 3.0$  and a random initial value  $(X_0, Y_0, Z_0)$ . Middle figure: the corresponding PD is computed by constructing V-R complex on the 3D data points. Right figure: the persistence grid is marked in red, and the persistence B-spline surface is reconstructed by the control grid.

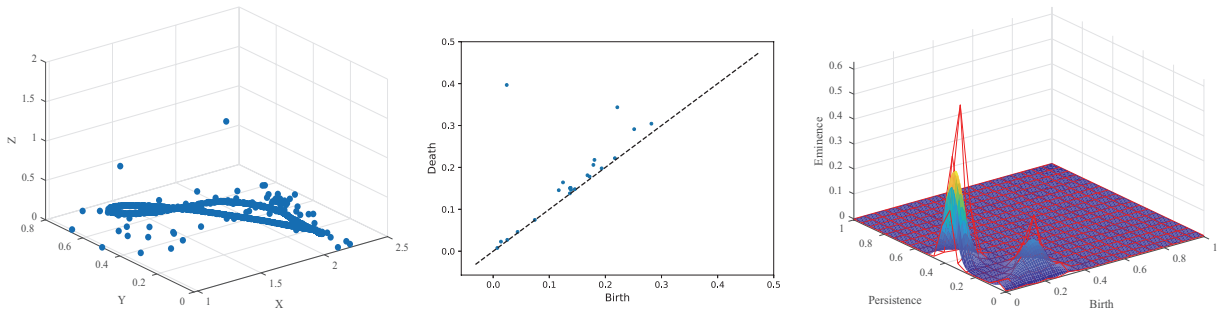


Figure 10: An example in the class of  $M_0 = 3.3$ . Left figure: the data points are generated by the 3D dynamical system with  $M_0 = 3.3$  and a random initial value  $(X_0, Y_0, Z_0)$ . Middle figure: the corresponding PD is computed by constructing V-R complex on the 3D data points. Right figure: the persistence grid is marked in red, and the persistence B-spline surface is reconstructed by the control grid.

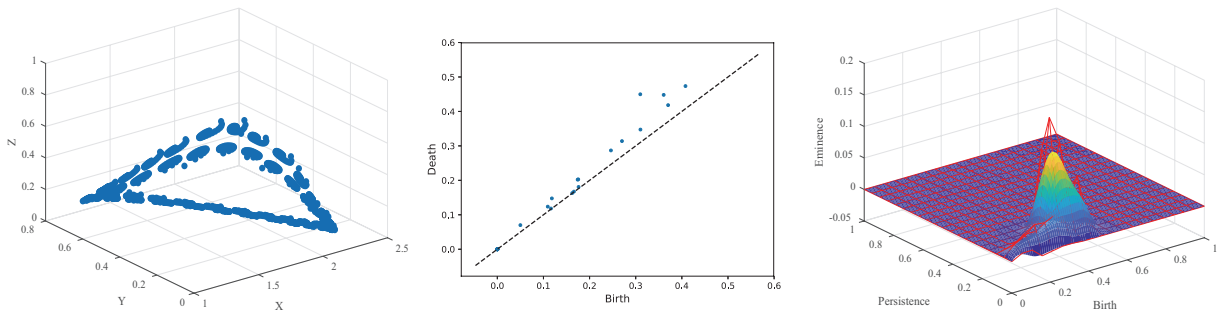


Figure 11: An example in the class of  $M_0 = 3.48$ . Left figure: the data points are generated by the 3D dynamical system with  $M_0 = 3.48$  and a random initial value  $(X_0, Y_0, Z_0)$ . Middle figure: the corresponding PD is computed by constructing V-R complex on the 3D data points. Right figure: the persistence grid is marked in red, and the persistence B-spline surface is reconstructed by the control grid.